

# 國立交通大學

## 材料科學與工程學系

### 碩士論文

Pt與 $\text{In}_2\text{O}_3$ 之修飾對於 $\text{TiO}_2$ 奈米線之光催化性質的影響

Effects of Pt and  $\text{In}_2\text{O}_3$  Decorations on the Photocatalytic Properties of

Anatase  $\text{TiO}_2$  Nanowires



研究生：陳宇志

指導教授：徐雍瑩 博士

中華民國九十九年七月

# Pt 與 $\text{In}_2\text{O}_3$ 之修飾對於 $\text{TiO}_2$ 奈米線之光催化性質的影響

學生：陳宇志

指導教授：徐雍瑩 博士

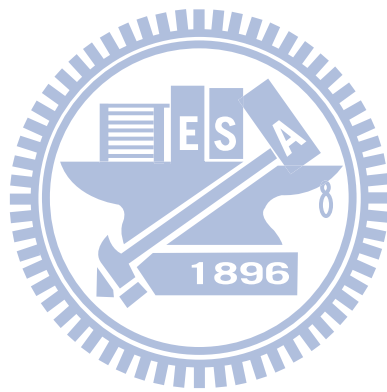
國立交通大學

材料科學與工程學系

## 中文摘要

透過結合不同能帶結構的半導體奈米晶體能提供許多的優點，如：更寬廣的吸收範圍、降低光漂白現象、能夠調控的能階和改善光電的轉換效率。在此論文中，我們透過沉積-鍛燒的方法成功合成出氧化銦修飾的銳鈦礦二氧化鈦奈米線 ( $\text{In}_2\text{O}_3$ - $\text{TiO}_2$  NWs)。由於氧化銦和二氧化鈦能帶結構的差異，使此複合材料能產生載子轉移，造成電子電洞對的分離。 $\text{In}_2\text{O}_3$ - $\text{TiO}_2$  奈米線內的載子分離特性，也展現在其降解染料的光催化的特性上。相較於商用的 P-25  $\text{TiO}_2$  粉末和利用物理方式混合的  $\text{In}_2\text{O}_3$ -loaded  $\text{TiO}_2$  NWs,  $\text{In}_2\text{O}_3$ - $\text{TiO}_2$  NWs 在紫外光的照射下，展現出更佳的光催化特性。為了更進一步提升其光催化活性，適量的 Pt 奈米粒子也被用來修飾在  $\text{In}_2\text{O}_3$ - $\text{TiO}_2$  NWs 上。這樣的提升是來自於在修飾 Pt 到二氧化鈦表面上之後，增加了電子由  $\text{In}_2\text{O}_3$  傳遞到  $\text{TiO}_2$  的驅動力。而且在自然陽光的照射下，顯示出  $\text{In}_2\text{O}_3$ - $\text{TiO}_2$ -Pt NWs 能

接收陽光中的能量進行高效率的光催化反應。電子在  $\text{In}_2\text{O}_3$ ,  $\text{TiO}_2$  和 Pt 的轉移現象，我們也透過其相對的光電流量測和時間解析螢光光光譜來探討分析。



Effects of Pt and In<sub>2</sub>O<sub>3</sub> Decorations on the Photocatalytic Properties of  
Anatase TiO<sub>2</sub> Nanowires

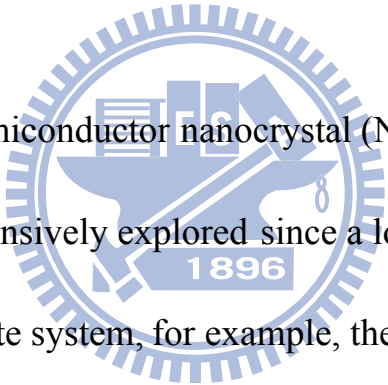
Student : Yu-Chih Chen

Advisors : Dr. Yung-Jung Hsu

National Chiao Tung University

Department of Materials Science and Engineering

**Abstract (in English)**



Combination of semiconductor nanocrystal (NCs) with different band structures has been extensively explored since a lot of advantages may be offered by this composite system, for example, the wide absorption profile, the enhanced resistance to photobleaching, the continuous tunability of energetic levels, and the improved photoelectric conversion efficiency. In this thesis, we successfully synthesized In<sub>2</sub>O<sub>3</sub>-decorated anatase TiO<sub>2</sub> nanowires (In<sub>2</sub>O<sub>3</sub>-TiO<sub>2</sub> NWs) through a simple precipitation-annealing process. The difference in band structures between In<sub>2</sub>O<sub>3</sub> and TiO<sub>2</sub> provided charge carriers with another preferential route for charge transfer, resulting in the separation of photoexcited electrons and holes.

The charge carrier separation in  $\text{In}_2\text{O}_3\text{-TiO}_2$  NWs was revealed with their photocatalytic decomposition toward an organic dye. As compared to the commercial P-25  $\text{TiO}_2$  powder and  $\text{In}_2\text{O}_3$ -loaded  $\text{TiO}_2$  NW samples, the as-synthesized  $\text{In}_2\text{O}_3\text{-TiO}_2$  NWs exhibited superior photocatalytic efficiency under UV illumination, demonstrating their potential as an efficient photocatalyst in relevant redox reactions. A further enhancement in the photocatalytic activity of  $\text{In}_2\text{O}_3\text{-TiO}_2$  NWs can be achieved when Pt nanoparticles of suitable amount were deposited on the surface of  $\text{TiO}_2$ . This improvement is due to the increasing driving force of electron transfer from  $\text{In}_2\text{O}_3$  to  $\text{TiO}_2$  achieved by the decoration of Pt on  $\text{TiO}_2$  surfaces. Furthermore, the result of performance evaluation under natural sunlight shows that the present  $\text{In}_2\text{O}_3\text{-TiO}_2\text{-Pt}$  NWs can be used as highly efficient photocatalysts which may practically harvest energy from sunlight. The electron transfer event among  $\text{In}_2\text{O}_3$ ,  $\text{TiO}_2$  and Pt was also characterized with the corresponding photocurrent measurement and time-resolved PL spectroscopy.

# 致謝

首先誠摯的感謝指導教授徐雍瑩博士，透過老師的提攜和指點，讓我這個初次觸碰半導體材料的學生，能夠順利進入奈米材料的領域裡，也得以對奈米領域有一定的認知了解。此外也感謝段興宇教授和黃暄益教授的批評和指教，讓我了解到自己對學問研究還有更多要改進的地方。

在此也要向實驗室的學長、學弟妹們表達感謝，有你們的幫助才能讓我順利完成本篇論文。感謝韋達、盈志、楹凱、耀德學長在實驗上給我的提點和幫助，使我面對實驗上的問題時都能得到解答。感謝眾多的學弟妹們，感謝你們常常幫我買午、晚餐，讓我能有更多的時間花費在研究上。還有感謝方郁歆同學和Ann，我們順利結束了兩年的碩士時光，祝你們畢業快樂。能夠認識實驗室的大家，我很幸運!!。最後也感謝我的家人，總是在背後支持我的決定，感謝你們。

# Table of Content

<b>Abstract (in Chinese)</b>	<b>I</b>
<b>Abstract (in English)</b>	<b>III</b>
<b>Acknowledgements</b>	<b>V</b>
<b>Figure Captions</b>	<b>VIII</b>
<b>Chapter 1. Introduction</b>	<b>1</b>
<b>1.1 Introduction of TiO<sub>2</sub></b> .....	<b>1</b>
<b>1.2 One-dimensional TiO<sub>2</sub> nanostructures</b> .....	<b>2</b>
<b>1.2.1 Previous Studies of 1-D TiO<sub>2</sub> nanostructures</b> .....	<b>4</b>
<b>1.2.2 Recently Studies of 1-D TiO<sub>2</sub> Nanostructures</b> .....	<b>7</b>
<b>1.3 Semiconductor-Metal Composite System</b> .....	<b>9</b>
<b>1.4 Semiconductor-Semiconductor Composite System</b> .....	<b>11</b>
<b>Chapter 2. Experimental Section</b>	<b>13</b>
<b>2.1 Chemicals</b> .....	<b>13</b>
<b>2.2 Instruments and Principles</b> .....	<b>13</b>
<b>2.3 Preparation of Anatase TiO<sub>2</sub> Nanowires</b> .....	<b>16</b>
<b>2.4 Preparation of Pt-decorated TiO<sub>2</sub> NWs</b> .....	<b>17</b>
<b>2.5 Preparation of In<sub>2</sub>O<sub>3</sub>-decorated TiO<sub>2</sub> NWs</b> .....	<b>18</b>

2.6 Preparation of Pt and In <sub>2</sub> O <sub>3</sub> co-decorated TiO <sub>2</sub> NWs .....	18
2.7 Photocurrent Measurement .....	19
2.8 Photocatalytic Activity Study .....	19
2.9 Photoluminescence Lifetime Measurement.....	20
2.10 Characterization .....	21
<b>Chapter 3. Results and Discussion</b>	<b>22</b>
3.1 Structural Investigation on TiO <sub>2</sub> NWs .....	22
3.2 Decoration of Pt on TiO <sub>2</sub> NWs.....	23
3.3 Photocatalytic Properties of Pt-decorated TiO <sub>2</sub> NWs .....	27
3.4 Effects of Various Metal Decorations and Recycling Test ....	30
3.5 Decoration of In <sub>2</sub> O <sub>3</sub> on TiO <sub>2</sub> NWs.....	33
3.6 Photocatalytic Properties of In <sub>2</sub> O <sub>3</sub> -decorated TiO <sub>2</sub> NWs .....	38
3.7 Further Decoration of Pt on In <sub>2</sub> O <sub>3</sub> -TiO <sub>2</sub> NWs .....	42
3.8 Photocatalytic Properties of In <sub>2</sub> O <sub>3</sub> -TiO <sub>2</sub> -Pt NWs .....	44
3.9 Photocurrent Measurement for In <sub>2</sub> O <sub>3</sub> -TiO <sub>2</sub> -Pt NWs .....	48
3.10 Time-Resolved Photoluminescence Spectra .....	52
<b>Chapter 4. Conclusion</b>	<b>58</b>
<b>Reference</b>	<b>60</b>



# Figure Captions

<b>Figure 1.1</b> List of bandgaps of common semiconductors.....	2
<b>Figure 1.2.1</b> Comparison of photocatalytic efficiency for TiO <sub>2</sub> nanorods with different aspect ratios. ....	3
<b>Figure 1.2.2</b> Morphological phase diagram of nanostructures of H <sub>2</sub> Ti <sub>3</sub> O <sub>7</sub> after 20 h of hydrothermal treatment.....	5
<b>Figure 1.2.3</b> TEM images of H <sub>2</sub> Ti <sub>3</sub> O <sub>7</sub> with (A) nanoparticle/nanotube mixture, (B) nanotubes, (C) nanotube/nanoribbon mixture, (D) and nanoribbons.....	6
<b>Figure 1.2.4</b> Schematic illustration for the formation mechanism of H <sub>2</sub> Ti <sub>3</sub> O <sub>7</sub> nanotubes.....	6
<b>Figure 1.2.5</b> (a) SEM image of H <sub>2</sub> Ti <sub>3</sub> O <sub>7</sub> NWs. (b,c,d) TEM and ED results of the anatase TiO <sub>2</sub> nanoshuttles. (e,f) TEM and the corresponding HRTEM images for a single shuttle .....	8
<b>Figure 1.2.6</b> TEM images of the TiO <sub>2</sub> products obtained with different hydrothermal reaction times: (a) 3 h, (b) 6 h.....	8
<b>Figure 1.3.1</b> Fermi level equilibration in a semiconductor-metal nanocomposite system.....	10

<b>Figure 1.3.2</b> (a) Typical TEM image, (b) ED pattern and (c) HRTEM image of Au-decorated $\text{Na}_x\text{H}_{2-x}\text{Ti}_3\text{O}_7$ NBs .....	10
<b>Figure 1.3.3</b> Photodegradation of thionine under visible irradiation by using Au-decorated $\text{Na}_x\text{H}_{2-x}\text{Ti}_3\text{O}_7$ NBs with various Au contents.....	11
<b>Figure 1.4.1</b> Charge carrier dynamis in a coupled semiconductor system. ....	12
<b>Figure 3.1.1</b> SEM images of (a) $\text{H}_2\text{Ti}_3\text{O}_7$ and (b) anatase $\text{TiO}_2$ NWs. (c) The corresponding XRD patterns.....	23
<b>Figure 3.2.1</b> (a) Typical TEM, (b) HRTEM and (c) EDS analyses of Pt-decorated $\text{TiO}_2$ NWs.....	26
<b>Figure 3.2.2</b> TEM images of Pt-decorated $\text{TiO}_2$ NWs with the Pt contents of (a) 1.0, (b) 2.0, (c) 3.0, (d) 5.0 and (e) 10 wt %.....	26
<b>Figure 3.3.1</b> Absorption spectra of MB solutions under different UV irradiation times by using $\text{TiO}_2$ NWs. ....	29
<b>Figure 3.3.2</b> $C/C_0$ versus irradiation time plots for MB photodegradation under UV illumination by using Pt-decorated $\text{TiO}_2$ NWs with various Pt contents.....	29

<b>Figure 3.4.1</b> The MB photodegradation results by using different photocatalysts including Pt-loaded, Pt-decorated, Ag-decorated, Au-decorated TiO <sub>2</sub> NWs, and P-25 TiO <sub>2</sub> powder .....	32
<b>Figure 3.4.2</b> Recycling test on Pt-decorated TiO <sub>2</sub> NWs with Pt content of 3 wt %.....	32
<b>Figure 3.5.1</b> SEM images of (a) In <sub>2</sub> O <sub>3</sub> -decorated TiO <sub>2</sub> NWs (molar ratio of In <sub>2</sub> O <sub>3</sub> to TiO <sub>2</sub> =1:1), and (b) pure In <sub>2</sub> O <sub>3</sub> nanoparticles.....	35
<b>Figure 3.5.2</b> SEM image of In(OH) <sub>3</sub> -decorated TiO <sub>2</sub> NWs.....	36
<b>Figure 3.5.3</b> HRTEM image taken on an individual In <sub>2</sub> O <sub>3</sub> -decorated TiO <sub>2</sub> NW .....	36
<b>Figure 3.5.4</b> In <sub>2</sub> O <sub>3</sub> -decorated TiO <sub>2</sub> NWs with various In <sub>2</sub> O <sub>3</sub> /TiO <sub>2</sub> molar ratios of (a) 0.25:1, (b) 0.5:1, (c) 1:1, (d)1.5:1, (e) 2:1, (f) 2.5:1 (g) 5:1 .....	37
<b>Figure 3.6.1</b> Absorption spectra of RB solutions under different UV irradiation times by using TiO <sub>2</sub> NWs. ....	39

<b>Figure 3.6.2</b> $C/C_0$ versus irradiation time plots for RB photodegradation under UV illumination by using $\text{In}_2\text{O}_3$ -decorated $\text{TiO}_2$ NWs with various $\text{In}_2\text{O}_3/\text{TiO}_2$ molar ratios .....	40
<b>Figure 3.6.3</b> The RB photodegradation results under UV light irradiation by using different photocatalysts including $\text{In}_2\text{O}_3$ -loaded, $\text{In}_2\text{O}_3$ -decorated, $\text{TiO}_2$ NWs and commercial P-25 $\text{TiO}_2$ powders.....	41
<b>Figure 3.6.4</b> Recycling test on $\text{In}_2\text{O}_3$ -decorated $\text{TiO}_2$ NWs with the $\text{In}_2\text{O}_3/\text{TiO}_2$ molar ratio of 1:1.....	42
<b>Figure 3.7.1</b> TEM image and the corresponding EDS spectra for $\text{In}_2\text{O}_3$ - $\text{TiO}_2$ -Pt NWs.....	44
<b>Figure 3.8.1</b> Band structures and charge transfer event in $\text{In}_2\text{O}_3$ - $\text{TiO}_2$ -Pt NWs. ....	46
<b>Figure 3.8.2</b> MB photodegradation results under UV light irradiation by using $\text{In}_2\text{O}_3$ - $\text{TiO}_2$ -Pt NWs with various Pt contents. ....	46
<b>Figure 3.8.3</b> Absorption spectra of MB solutions after exposure of 1 h of daytime sunlight (a) without any catalyst and (b) in the presence of $\text{In}_2\text{O}_3$ - $\text{TiO}_2$ -Pt NWs. ....	48

<b>Figure 3.9.1</b> Photocurrent response of pure TiO <sub>2</sub> NWs, In <sub>2</sub> O <sub>3</sub> -TiO <sub>2</sub> NWs and In <sub>2</sub> O <sub>3</sub> -TiO <sub>2</sub> -Pt NWs with differernt Pt contents.....	50
<b>Figure 3.9.2</b> Illustration of the apparent Fermi level potential of TiO <sub>2</sub> in (a) In <sub>2</sub> O <sub>3</sub> -TiO <sub>2</sub> and (b) In <sub>2</sub> O <sub>3</sub> -TiO <sub>2</sub> -Pt systems. ....	51
<b>Figure 3.10.1</b> Charge separation scheme for Pt/In <sub>2</sub> O <sub>3</sub> /TiO <sub>2</sub> in present of RB dye. ....	53
<b>Figure 3.10.2</b> Quenching of photoluminescence emission of RB Dye (doner) with different samples (acceptors).....	53
<b>Figure 3.10.3</b> Time-resolved PL spectra of RB solutions containing In <sub>2</sub> O <sub>3</sub> , In <sub>2</sub> O <sub>3</sub> -TiO <sub>2</sub> and In <sub>2</sub> O <sub>3</sub> -TiO <sub>2</sub> -Pt samples. ....	56
<b>Table 1</b> Kinetic analysis of emission decay of RB in the presence of different samples.....	57

# Chapter 1. Introduction

## 1.1 Introduction of TiO<sub>2</sub>

Titanium dioxide (TiO<sub>2</sub>) has been widely employed as photocatalytic materials in the purification and treatment of contaminated air and water owing to its low cost, nontoxicity, and chemical stability [1]. Recently, one-dimensional nanostructures of TiO<sub>2</sub> such as nanotubes and nanowires have attracted intensive research interests because of their dimensionality-dependent physicochemical properties and potential applications in the fields of solar-energy conversion, lithium batteries, and supercapacitors. TiO<sub>2</sub> exists in nature as well-known minerals of rutile, anatase and brookite. Anatase is metastable with respect to rutile and may transform spontaneously into rutile at temperature above 800 °C [2]. As shown in Figure 1.1, anatase TiO<sub>2</sub> possesses relatively negative conduction band potential that ensures promising activity in many photocatalytic processes. However, its wide bandgap energy (3.2 eV) allows only ultraviolet (UV) absorption. As a result, an effort to modulate the band structure of TiO<sub>2</sub> to enable photocatalysis under visible light is being pursued.

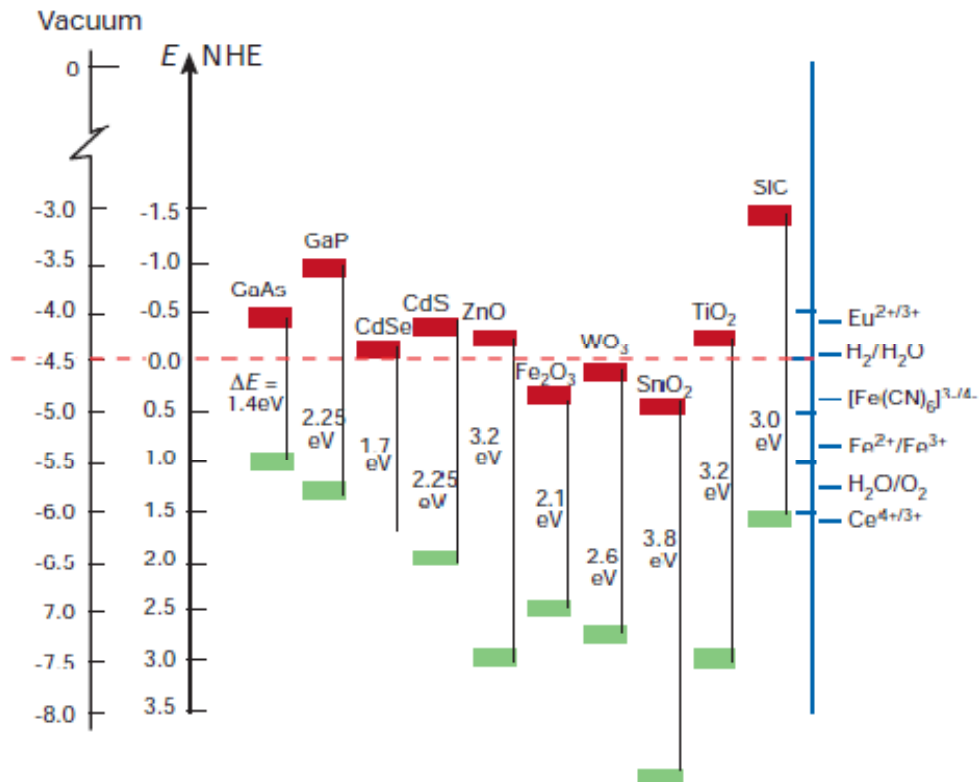


**Figure 1.1** List of bandgaps of common semiconductors [3].

## 1.2 One-dimensional $\text{TiO}_2$ nanostructures

One-dimensional (1-D) nanostructures including nanowires, nanorods, nanoribbons and nanotubes have been the subject of intensive research due to their potential use as active components or interconnects in nanoscale electronic and electromechanical devices [4]. The space charge region in 1-D nanostructured crystals is well constructed along the longitudinal direction, enabling charge transfer along single direction and thus the facilitation of carrier collections. Furthermore, the pronounced delocalization of charge carriers in 1-D crystals can significantly lower

the probability of  $e^-h^+$  recombination [5]. Consequently, improved photoelectric conversion efficiency such as the photocatalytic activity was regularly observed in 1-D nanostructures when compared with their spherical or particulate counterparts. As shown in Figure 1.2.1,  $TiO_2$  nanorods with higher aspect ratios were found to exhibit superior photocatalytic performance as compared to the nanoparticles and short nanorods [5].

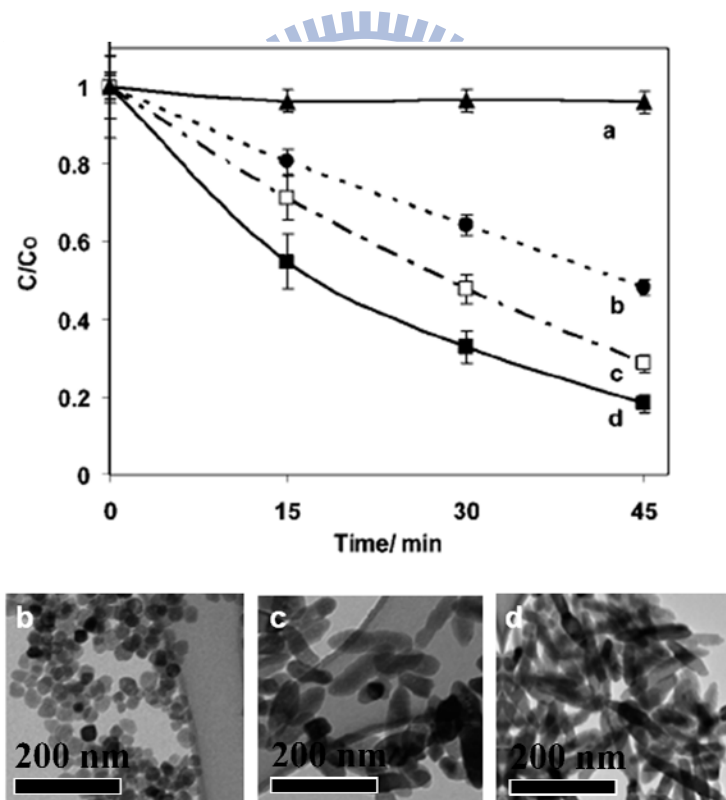


**Figure 1.2.1** Comparison of photocatalytic efficiency for  $TiO_2$  nanorods with different aspect ratios [5].



### 1.2.1 Previous Studies of 1-D TiO<sub>2</sub> nanostructures

There are many synthetic methods to obtain TiO<sub>2</sub> in 1-D forms, such as sol-gel method [6, 7], hydrothermal method [8], solvothermal method [9], direct oxidation process [10], chemical vapor deposition [11], electrochemical deposition [12], and sonochemical method [13]. As one of the Ti-O series products, hydrogen titanate (H<sub>2</sub>Ti<sub>3</sub>O<sub>7</sub>) has drawn much research attention due to its capability of feasible transformation into 1-D TiO<sub>2</sub> upon heat treatment. Since the pioneering work by Kasuga et al [14, 15], alkaline hydrothermal approach has been widely employed to produce H<sub>2</sub>Ti<sub>3</sub>O<sub>7</sub>. By using P-25 TiO<sub>2</sub> powder as the precursor in concentrated NaOH solution, various 1-D H<sub>2</sub>Ti<sub>3</sub>O<sub>7</sub> including nanotubes, nanosheets, nanowires and nanoribbons can be obtained in high yield. As revealed in Figure 1.2.2, the morphology of H<sub>2</sub>Ti<sub>3</sub>O<sub>7</sub> in the alkaline hydrothermal process can be readily controlled by modulating the concentration of NaOH and the reaction temperature. Figure 1.2.3 shows the TEM images of the as-obtained H<sub>2</sub>Ti<sub>3</sub>O<sub>7</sub> products by using the alkaline hydrothermal method. A formation mechanism for these 1-D nanostructures of H<sub>2</sub>Ti<sub>3</sub>O<sub>7</sub> was proposed and illustrated in Figure 1.2.4 [17]. At the beginning of reaction, anatase crystallites of P-25 TiO<sub>2</sub>

partially dissolved in NaOH, leaving terraces on their surface. The dissolved atoms recrystallized in sheet-like structures, which further curved up into nanoloops with single-spiral, multiple-spiral, or onion-like cross section. The rest of the bulk crystal was then transformed into nanotubes by oriented crystal growth, supplied with  $\text{TiO}_6$  building blocks via the alkaline dismantling of the anatase raw material of  $\text{TiO}_2$ .

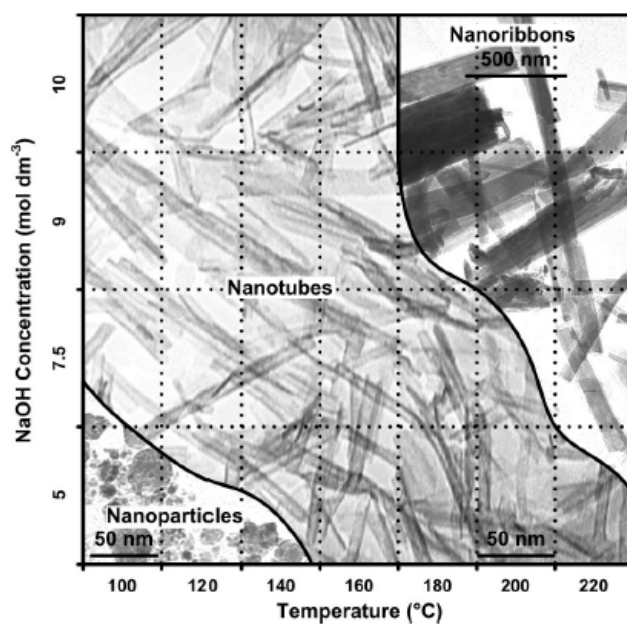


**Figure 1.2.2** Morphological phase diagram of nanostructures of  $\text{H}_2\text{Ti}_3\text{O}_7$  after 20 h of hydrothermal treatment [16].

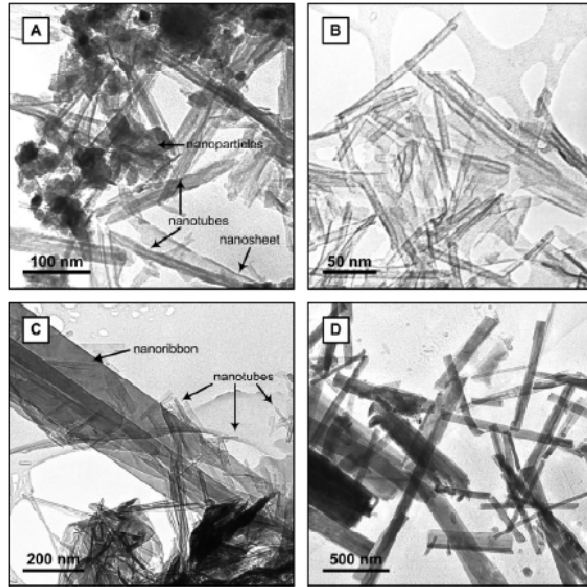


**Figure 1.2.3** TEM images of  $\text{H}_2\text{Ti}_3\text{O}_7$  with (A) nanoparticle/nanotube mixture, (B) nanotubes, (C) nanotube/nanoribbon mixture, (D) and nanoribbons. Conditions of reaction: (A) 5 mol  $\text{dm}^{-3}$  of NaOH at 140 °C, (B) 9 mol  $\text{dm}^{-3}$  of NaOH at 160 °C, (C) 5 mol  $\text{dm}^{-3}$  of NaOH at 220 °C, and (D) 7.5 mol  $\text{dm}^{-3}$  of NaOH at 220 °C [16].

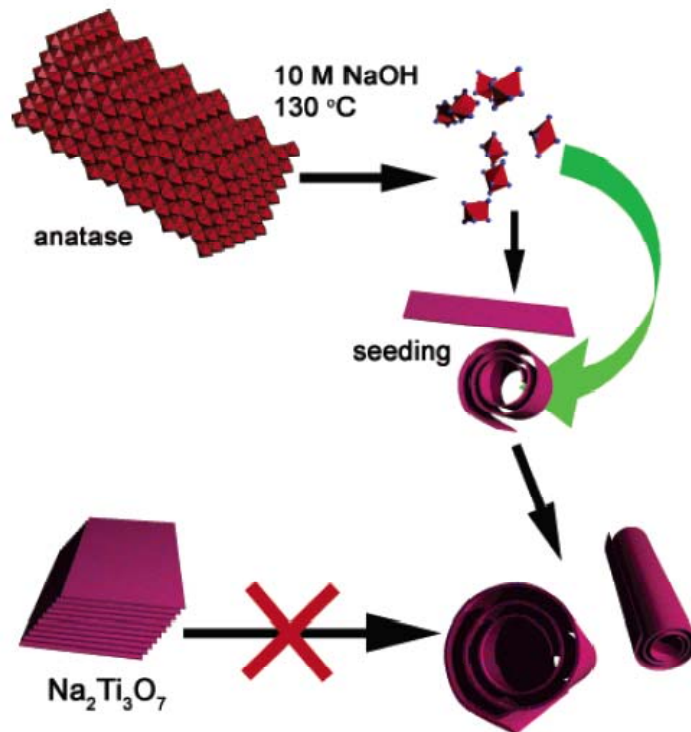


**Figure 1.2.4** Schematic illustration for the formation mechanism of  $\text{H}_2\text{Ti}_3\text{O}_7$  nanotubes [17].

## 1.2.2 Recently Studies of 1-D TiO<sub>2</sub> Nanostructures

With the open-ended tabulate and layered structures, H<sub>2</sub>Ti<sub>3</sub>O<sub>7</sub> has been shown promising in the preparation of diverse 1-D TiO<sub>2</sub> nanostructures. Recently, Wang et al successfully synthesized anatase TiO<sub>2</sub> nanoshuttles through the hydrothermal treatment on the first-prepared H<sub>2</sub>Ti<sub>3</sub>O<sub>7</sub> NWs [18]. Figure 1.2.5 displays the TEM images of TiO<sub>2</sub> nanoshuttles obtained by controlling the pH value of the reaction solution. Due to the minimization of total surface energies, TiO<sub>2</sub> nanoshuttles were grown with the thermodynamically stable facets of (101) and (001) exposed at their surfaces. The morphology of the final products can be further modulated by controlling the hydrothermal reaction time. As shown in Figure 1.2.6, fishbone-like composite structures can be obtained by prolonging the reaction time to 3 and 6 h. These delicate structures may find practical applications in photocatalysts.

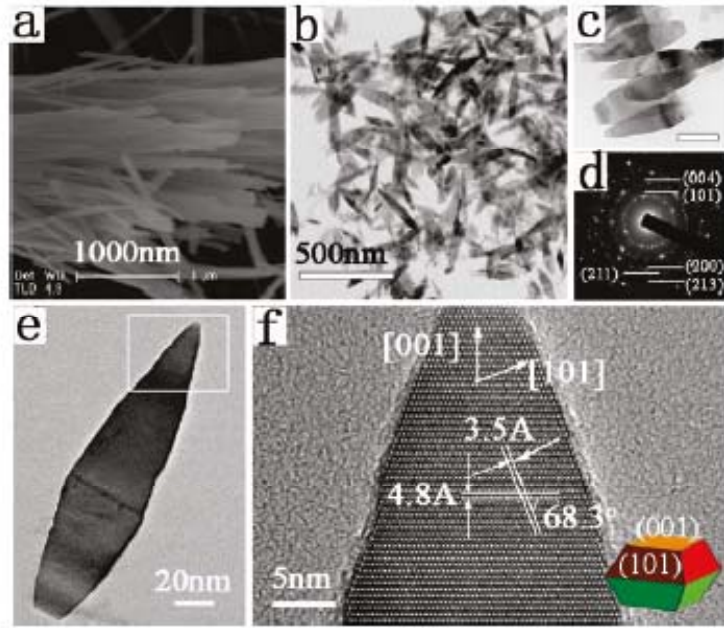


**Figure 1.2.5** (a) SEM image of  $\text{H}_2\text{Ti}_3\text{O}_7$  NWs. (b,c,d) TEM and ED results of the anatase  $\text{TiO}_2$  nanoshuttles. (e,f) TEM and the corresponding HRTEM images for a single shuttle [18].

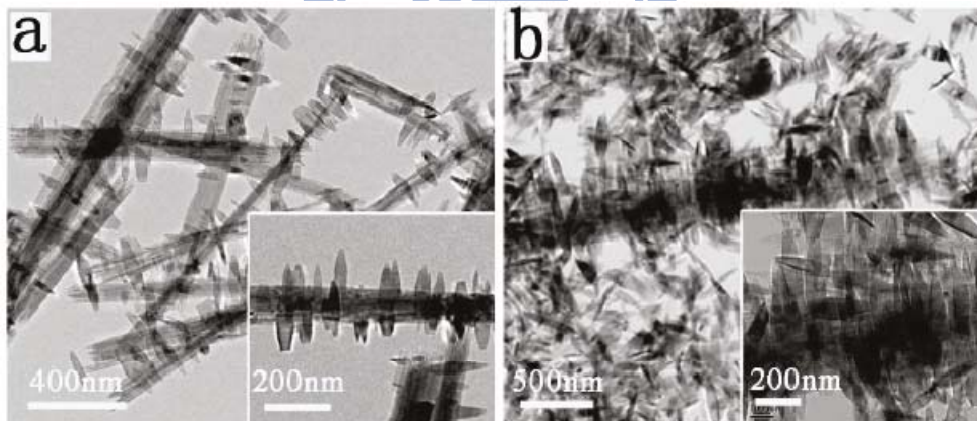


**Figure 1.2.6** TEM images of the  $\text{TiO}_2$  products obtained with different hydrothermal reaction times: (a) 3 h, (b) 6 h [18].

### 1.3 Semiconductor-Metal Composite System

Semiconductor-metal nanocomposites have been widely employed in photocatalysis [19-21]. The overall photocatalytic efficiency of semiconductors can be enhanced by contacting with metals. When semiconductor and metal nanoparticles are in contact, the photoexcited charge carriers re-distribute between the semiconductor and metal domains [22]. This phenomenon promotes the separation of electron-hole pairs. Figure 1.3.1 displays the Fermi level equilibration in a semiconductor-metal nanocomposite system. Within this system, metal may play an important role of storing and shuttling electrons. The photogenerated electrons of semiconductor would thus preferentially transfer to metal domain, leaving positively charged holes in semiconductor to achieve charge carrier separation [23]. Pu et al recently reported a semiconductor-metal composite system of Au-decorated  $\text{Na}_x\text{H}_{2-x}\text{Ti}_3\text{O}_7$  nanobelts (NBs). The morphological investigation was shown in Figure 1.3.2 [24]. Due to the band offsets between  $\text{Na}_x\text{H}_{2-x}\text{Ti}_3\text{O}_7$  and Au, a notable charge separation was expected to take place at the interface of  $\text{Na}_x\text{H}_{2-x}\text{Ti}_3\text{O}_7/\text{Au}$ , leading to the enhanced photocatalytic efficiency observed for Au-decorated  $\text{Na}_x\text{H}_{2-x}\text{Ti}_3\text{O}_7$  NBs (Figure 1.3.3).

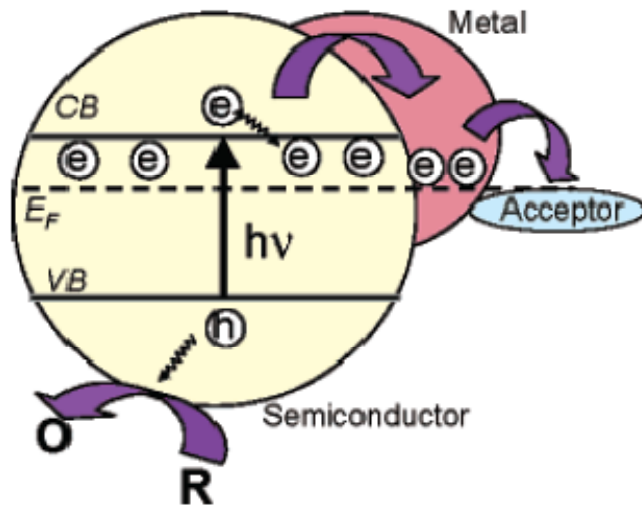


**Figure 1.3.1** Fermi level equilibration in a semiconductor-metal nanocomposite system [22]

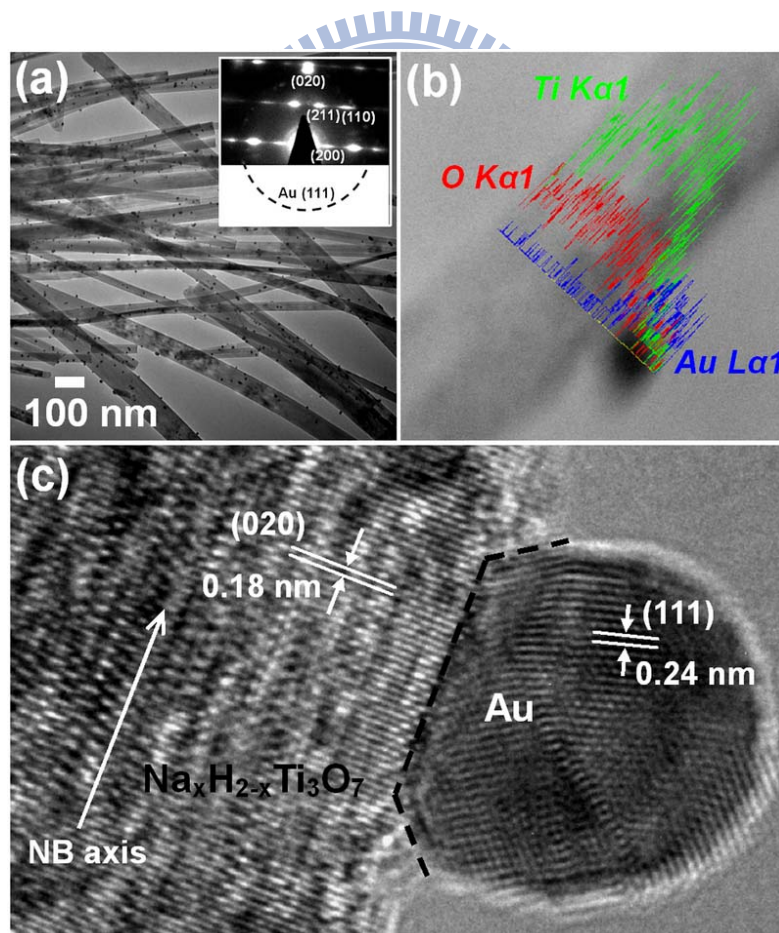


**Figure 1.3.2** (a) Typical TEM image, (b) ED pattern and (c) HRTEM image of Au-decorated  $\text{Na}_x\text{H}_{2-x}\text{Ti}_3\text{O}_7$  NBs [24].

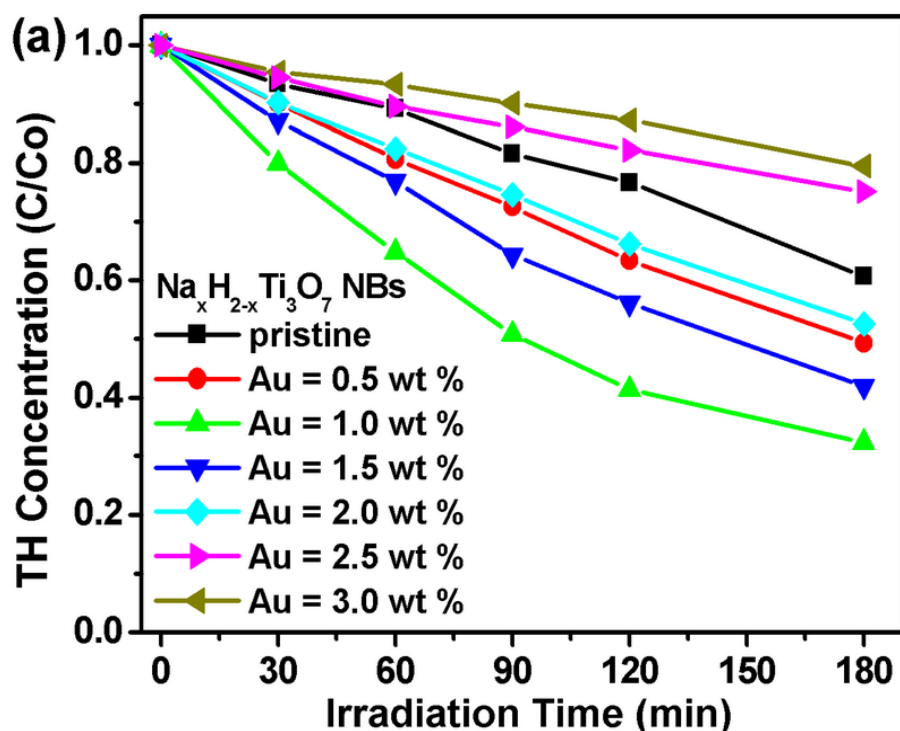


**Figure 1.3.3** Photodegradation of thionine under visible irradiation by using Au-decorated  $\text{Na}_x\text{H}_{2-x}\text{Ti}_3\text{O}_7$  NBs with various Au contents. [24]

## 1.4 Semiconductor-Semiconductor Composite System

Besides the semiconductor-metal composite system, combination of two semiconductors with appropriate band offsets (type-II heterogeneity) may also improve the charge carrier separation. Kamat et al studied the photoelectrochemical behavior of CdSe/TiO<sub>2</sub> composite films and found an increased photocurrent over the electrode [25]. As shown in Figure 1.4.1, upon light illumination, the photogenerated electrons quickly transferred from CdSe to TiO<sub>2</sub> due to the lower conduction band potential of TiO<sub>2</sub>. The photogenerated holes simultaneously migrated to the



interface of CdSe/solution, allowing for oxidation reaction with the redox couple of solution. Combining two different semiconductors has two main advantages: (1) extension of light absorption in a wider range, and (2) retardation of charge carrier recombination.

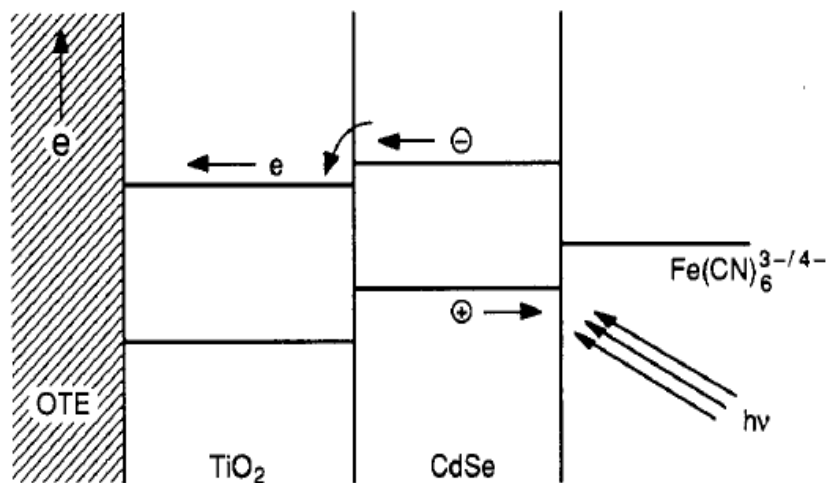


**Figure 1.4.1** Charge carrier dynamics in a coupled semiconductor system [25].

# Chapter 2. Experimental Section

## 2.1 Chemicals

All chemicals were analytic grade reagents and used without further purification.

1. P-25 ( $\text{TiO}_2$ ), Degussa.
2. Sodium hydroxide ( $\text{NaOH}$ ), 99.995%, Aldrich.
3. Ethanol ( $\text{CH}_3\text{CH}_2\text{OH}$ ), 99.5%, Aldrich.
4. Chloroplatinic acid hydrate ( $\text{H}_2\text{PtCl}_6$ ), 99.995%, Aldrich.
5. Indium (III) chloride ( $\text{InCl}_3$ ), 99.99%, Aldrich.
6. Ammonium hydroxide solution ( $\text{NH}_4\text{OH}$ ), 33%, Aldrich.
7. Chloroauric acid ( $\text{HAuCl}_4$ ), 99.99%, Aldrich.
8. Silver nitrate ( $\text{AgNO}_3$ ), 99.99%, J.T Baker.
9. Methylene blue, ( $\text{C}_{16}\text{H}_{18}\text{N}_3\text{SCl} \cdot 3\text{H}_2\text{O}$ ), Aldrich.
10. Rhodamine B, ( $\text{C}_{28}\text{H}_{31}\text{ClN}_2\text{O}_3$ ), Aldrich.

## 2.2 Instruments and Principles

1. Scanning Electron Microscope (SEM): The kinetic energy of accelerated electrons in SEM is dissipated as many different signals when hitting the sample surfaces. These signals mainly include

secondary and backscattered electrons. Secondary and backscattered electrons are then collected and used for imaging the morphology and compositional contrast of samples, respectively.

2. Transmission Electron Microscope (TEM): In TEM, the electrons are focused with electromagnetic lenses and transmitted through the sample to image and analyze the microstructure. The electron beams are basically accelerated at several hundred kV, producing wavelength much smaller than that of light. For example, 200 kV of acceleration voltage produces electron beam with a wavelength of  $0.025\text{\AA}$ . The resolution of TEM is however limited by aberrations inherent in electromagnetic lenses, which is about  $1\text{-}2\text{\AA}$ .
3. Energy-Dispersive X-Ray Spectroscopy (EDS): EDS is a typical facility of SEM and TEM. It includes a sensitive X-ray detector, a liquid nitrogen cooling system, and software to analyze the energy spectra. An EDS detector contains a crystal that absorbs X-ray by ionization, yielding free electrons in the crystal to produce an electrical charge bias. The signals are then converted into the characteristic X-ray of element to identify the composition of samples.
4. X-Ray Diffraction (XRD): In XRD, a constructive interference is

produced through the interaction of the incident X-ray with the sample under the regime of Bragg's Law ( $n\lambda = 2d \sin \theta$ ). This law correlates the wavelength of X-ray ( $\lambda$ ) with the diffraction angle ( $2\theta$ ) and the lattice spacing of crystal ( $d$ ) of the sample. By scanning the sample through a wide  $2\theta$  range to collect primary diffraction peaks, one may identify the crystal structure of sample by referring to the standard reference patterns.

5. UV-Visible Spectrophotometer: Absorption of incident radiation by the electrons in materials usually leads to a high frequency, i.e. low wavelength, absorption band that can be observed in the range of 200 to 800 nm. For a solution containing an absorbing substance, the absorptivity ratio at a fixed wavelength is defined as  $I_0/I$ , which is logarithmically related to the concentration of solute ( $c$ ) and the optical path length of sample cell ( $b$ ) according to the Beer Lambert law: Absorbance ( $A$ ) =  $\log_{10}(I_0/I) = \alpha b c$ , where  $\alpha$  is a constant named absorption coefficient.
6. Photoluminescence Spectroscope: When materials are exposed to X-ray,  $\gamma$ - ray or light with sufficiently high energy, ionization of atoms takes place to remove the electrons from their orbits, rendering

the electronic structure of the atoms unstable. The electrons in higher orbit may then "fall" into the lower one to fill the hole left behind.

During the falling process, energy with an equal amount to the energetic difference between the two orbits will be released in the form of photon to emit radiation.

### **2.3 Preparation of Anatase TiO<sub>2</sub> Nanowires**

Commercial TiO<sub>2</sub> powder (Degussa P-25) was used as the starting material. In a typical process, 1.0 g of Degussa P-25 was first dispersed in 10 mL of absolute ethanol, and then mixed with 10 mL of 10 M NaOH aqueous solution under vigorous stirring for 10 min. The mixed solution was transferred into a Teflon-line stainless-steel autoclave. Subsequently, the autoclave was heated and maintained at 200°C for 24 h, and then cooled to room temperature naturally. The resultant white slurry was washed with deionized water and HCl aqueous solution (pH=1) until the pH value is below 7. A complete removal of Na constituent can be achieved through this acid-washing process [26], which resulted in the formation of H<sub>2</sub>Ti<sub>3</sub>O<sub>7</sub> NWs. These NWs were then annealed in air at 700 °C for 4 h to obtain anatase TiO<sub>2</sub> NWs.

## 2.4 Preparation of Pt-decorated TiO<sub>2</sub> NWs

To decorate NWs with Pt nanoparticles, 5 mg of anatase TiO<sub>2</sub> NWs were dispersed in 20 mL absolute ethanol, followed by the addition of 50 μL H<sub>2</sub>PtCl<sub>6</sub> (5 mM) with vigorous stirring. The mixed solution in quartz tube was irradiated by UV light (with the wavelength of 365 nm) for 30 min to generate electrons for reduction of Pt ions. Note that ethanol was used as the sacrificial reagent for the photogenerated holes. The product (TiO<sub>2</sub>-Pt NWs with the Pt content of 1.0 wt %) was centrifuged, washed with deionized water and ethanol, and then dried at 60°C in air. In this work, two other novel metals (Ag and Au) were also deposited on NW surfaces, with which we may learn the effects of various metal decorations on the photocatalytic properties of TiO<sub>2</sub>. For the synthesis of Au-decorated anatase TiO<sub>2</sub> NWs, HAuCl<sub>4</sub> was used as the Au source, followed by the same procedure performed in the preparation of Pt-decorated sample. As to the fabrication of Ag-decorated anatase TiO<sub>2</sub> NWs, AgNO<sub>3</sub> was used as the Ag source, followed by the same procedure mentioned above.

## 2.5 Preparation of In<sub>2</sub>O<sub>3</sub>-decorated TiO<sub>2</sub> NWs

To prepare In<sub>2</sub>O<sub>3</sub>-decorated TiO<sub>2</sub> NWs, 221.18 mg of InCl<sub>3</sub> powder was first dissolved in 5 mL deionized water, followed by the addition of 500  $\mu$ L NH<sub>4</sub>OH solution. After stirring for 10 min, TiO<sub>2</sub> NWs of 40 mg were added into the above solution. The mixed solution was then stirred for 12 h at room temperature. The resultant white precipitation was collected and washed with deionized water for several times. After dried in air at 60 °C, the white powder was further annealed in air at 700 °C for 2 h to produce In<sub>2</sub>O<sub>3</sub>-decorated TiO<sub>2</sub> NWs (In<sub>2</sub>O<sub>3</sub>-TiO<sub>2</sub>).

## 2.6 Preparation of Pt and In<sub>2</sub>O<sub>3</sub> co-decorated TiO<sub>2</sub> NWs

To prepare the Pt and In<sub>2</sub>O<sub>3</sub> co-decorated TiO<sub>2</sub> NWs, 5 mg of In<sub>2</sub>O<sub>3</sub>-TiO<sub>2</sub> NWs were dispersed in 20 mL absolute ethanol in a quartz tube first. H<sub>2</sub>PtCl<sub>6</sub> of a suitable amount (5 mM) was then added into the quartz tubes and irradiated by UV light (with the wavelength of 365 nm) for 30 min to grow Pt nanoparticles on the surfaces of TiO<sub>2</sub>. The product was centrifuged, washed with deionized water and ethanol, and then dried at 60 °C in air.

## 2.7 Photocurrent Measurement

Photocurrent measurement was conducted in a photoelectrochemical system under white light irradiation (xenon lamp, 500 W, with a light intensity of 175 mW/cm<sup>2</sup>). NW film, well adhered to FTO substrates, was prepared by dripping NW suspensions of sufficient amount onto FTO glasses, followed by a heat treatment to remove the solvent. The NW film on FTO substrate was used as the photoanode in the three-electrode cell which consisted of Pt counter electrode, Ag/AgCl reference electrode, and 0.01 M NaOH redox couple.

## 2.8 Photocatalytic Activity Study

Photodegradation of ethylene blue (MB) and rhoamine B (RB) were monitored to test the photocatalytic activity of the NW samples. Irradiation was provided by UV lamps (8W) with a wavelength of 365 nm. In a typical experiment, 5.0 mg of photocatalyst was added into 20 mL of MB (or RB) solution in the photoreactor vessel. The concentrations of MB and RB in the presence of NWs under illumination were both  $1.0 \times 10^{-5}$  M. At certain time intervals of irradiation, 1.5 mL of the reaction solution was withdrawn and centrifuged to remove the photocatalyst particles. The filtrates were



analyzed with a UV-Visible spectrophotometer to measure the concentration variation of dye through recording the corresponding absorbance of the characteristic peak. To investigate the recyclability and stability of photocatalysts, three cycles of photocatalytic reactions were conducted by using In<sub>2</sub>O<sub>3</sub>-TiO<sub>2</sub>-Pt NWs with the Pt content of 5.0 wt % as the representative sample. The photodegradation of MB ( $1.0 \times 10^{-5}$  M) under natural sunlight was also examined.

## 2.9 Photoluminescence Lifetime Measurement

Time-resolved photoluminescence (PL) spectra were measured using a home-built single photon counting system. Diode laser (375 nm) with the pulse duration of 50 ps was used as the excitation source. The signals collected at the excitonic emission of RB ( $\lambda = 581$  nm) were dispersed with a grating spectrometer, detected by a high-speed photomultiplier tube, and then correlated using a single photon counting card. The emission decay data were analyzed with the biexponential kinetics in which two decay components were derived. The lifetimes ( $\tau_1$  and  $\tau_2$ ), pre-exponential factors ( $A_1$  and  $A_2$ ), and intensity-average lifetime ( $\langle \tau \rangle$ ) were determined and

summarized for RB ( $1\mu\text{M}$ ), RB/ $\text{In}_2\text{O}_3$  (1mg in  $1\mu\text{M}$  RB), RB/ $\text{In}_2\text{O}_3$ - $\text{TiO}_2$  (2mg in  $1\mu\text{M}$  RB) and RB/  $\text{In}_2\text{O}_3$ - $\text{TiO}_2$ -Pt (2mg in  $1\mu\text{M}$  RB).

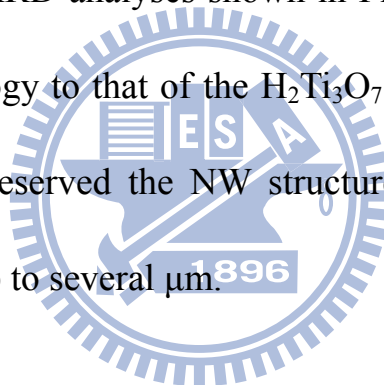
## 2.10 Characterization

The morphology and dimensions of the products were examined with a field-emission SEM (FESEM, JEOL, JSM-6500F). The crystallographic structure of the samples was investigated with XRD (Burker, D2 phaser) and a high-resolution TEM (HRTEM, JEOL, JEM-2010) operated at 200 kV. The compositional information was obtained with an EDS, an accessory of the TEM (JEM-2010). UV-Visible absorption spectra were obtained using a Hitachi U-3900H at  $25^\circ\text{C}$  under ambient atmosphere. For PL spectroscopy, a Hitachi F-4500 equipped with a xenon lamp (150W) was used. Photocurrent measurement for the  $\text{TiO}_2$  NWs film was measured by using an electrochemical workstation (Jiehan 5600, Taiwan) under a xenon lamp ( $500\text{W}$ ,  $175\text{mW}/\text{cm}^2$ ) illumination.

# Chapter 3. Results and Discussion

## 3.1 Structural Investigation on TiO<sub>2</sub> NWs

Figure 3.1.1 shows the SEM images and XRD patterns of H<sub>2</sub>Ti<sub>3</sub>O<sub>7</sub> and anatase TiO<sub>2</sub> NWs. The as-prepared H<sub>2</sub>Ti<sub>3</sub>O<sub>7</sub> NWs have a typical diameter of 70-150 nm and length up to a few μm. After calcinated at 700<sup>o</sup>C for 4h, a dehydration reaction occurred to H<sub>2</sub>Ti<sub>3</sub>O<sub>7</sub>, resulting in the formation of anatase TiO<sub>2</sub>. This phase transformation can be confirmed by the corresponding XRD analyses shown in Figure 3.1.1(c) [27]. Note that a similar morphology to that of the H<sub>2</sub>Ti<sub>3</sub>O<sub>7</sub> NWs was found for the anatase TiO<sub>2</sub> which preserved the NW structures with the diameter of 30-70 nm and length up to several μm.



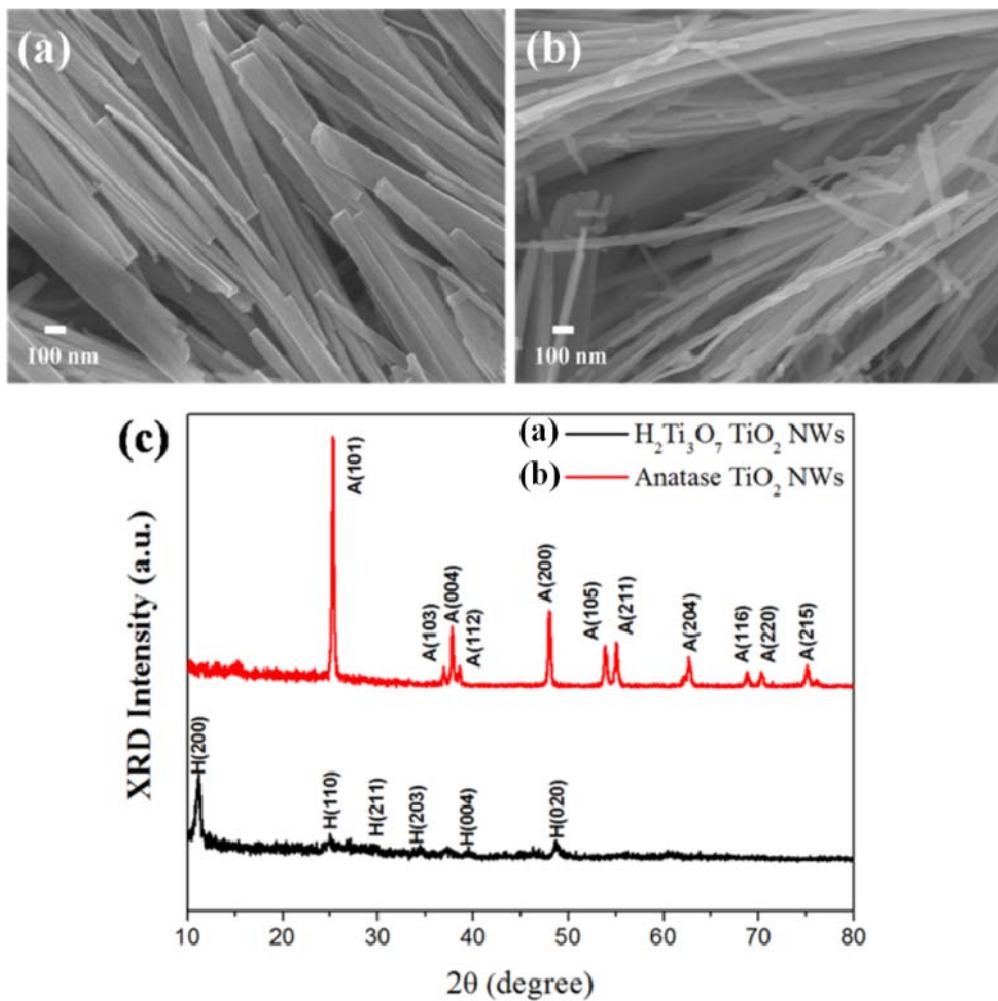


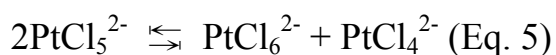
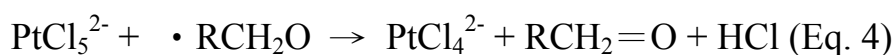
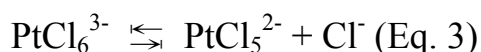
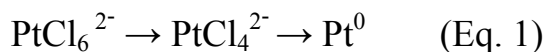
**Figure 3.1.1** SEM images of (a)  $\text{H}_2\text{Ti}_3\text{O}_7$  and (b) anatase  $\text{TiO}_2$  NWs. (c) The corresponding XRD patterns.

### 3.2 Decoration of Pt on $\text{TiO}_2$ NWs

To extract the photoexcited electrons from  $\text{TiO}_2$  NWs for participation in photocatalytic reduction reaction, we introduced an electron-acceptor, Pt, at the surfaces of NWs. We used the photodeposition method to deposit Pt nanoparticles onto  $\text{TiO}_2$  NWs. As shown in Figure 3.2.1 (a), Pt nanoparticles with a size of 2-5 nm were

presented on NW surfaces after the photodeposition process. The HRTEM image, shown in Figure 3.2.1 (b), clearly reveals an interlayer spacing of 1.89 Å in the NW region, in good agreement with the  $d$  spacing of the (200) lattice planes of anatase TiO<sub>2</sub> [28]. In the particle region, an interlayer spacing of 1.93 Å was obtained, complying with the lattice spacing of (200) planes of the fcc Pt [29]. With increasing the amount of H<sub>2</sub>PtCl<sub>6</sub>, the density of Pt nanoparticles grown at the surfaces of NWs was gradually increased (Figure 3.2.2). These Pt nanoparticles however have irregular shape and would aggregate once the concentration of H<sub>2</sub>PtCl<sub>6</sub> becomes relatively high. It should be noted that no free-standing Pt nanoparticles were observed in the products, demonstrating the advantage of the current approach to obtain metal nanoparticle-decorated NWs. A growth mechanism for the formation of Pt nanoparticles was proposed as follows (equations 1 to 5) [30-32]. Irradiation for PtCl<sub>6</sub><sup>2-</sup> ions under UV light would transform them into PtCl<sub>4</sub><sup>2-</sup> and then Pt<sup>0</sup> (equation 1). The photodeposition process of Pt on NWs mainly followed the three steps: (1) transformation of PtCl<sub>6</sub><sup>2-</sup> into PtCl<sub>4</sub><sup>2-</sup>, (2) dissociation of Cl from PtCl<sub>4</sub><sup>2-</sup>, followed by the reduction of Pt<sup>2+</sup> to Pt<sup>0</sup>, (3) formation of Pt<sup>0</sup>-Pt<sup>0</sup> bonds and particle growth by the

association of Pt<sup>0</sup>-Pt<sup>0</sup> [32]. Here ethanol plays an important role of accepting photogenerated holes of NWs and facilitating the formation of PtCl<sub>4</sub><sup>2-</sup> (equations 2 to 5) [31].



Based on the above interpretation, we believed that the present photodeposition approach can be extended to obtain other novel metal-decorated NWs such as Ag- and Au-decorated samples [33-35]. With these samples, we may learn the effects of various metal decorations on the photocatalytic properties of TiO<sub>2</sub> NWs.

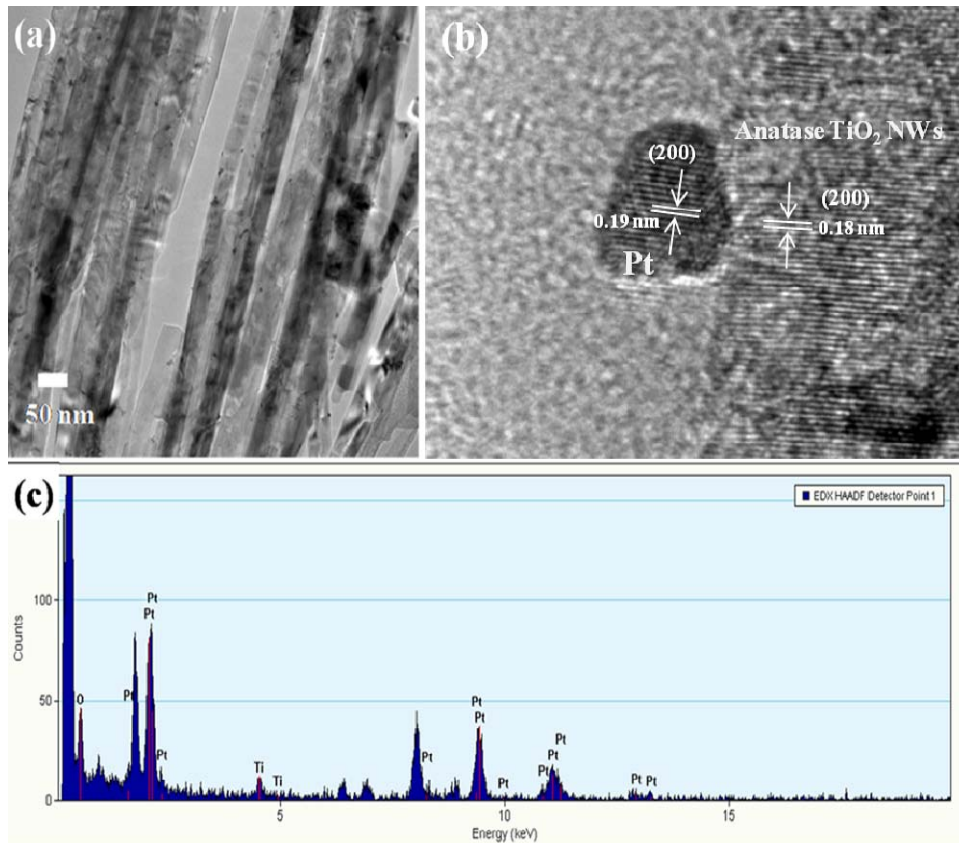


**Figure 3.2.1** (a) Typical TEM, (b) HRTEM and (c) EDS analyses of Pt-decorated TiO<sub>2</sub> NWs.

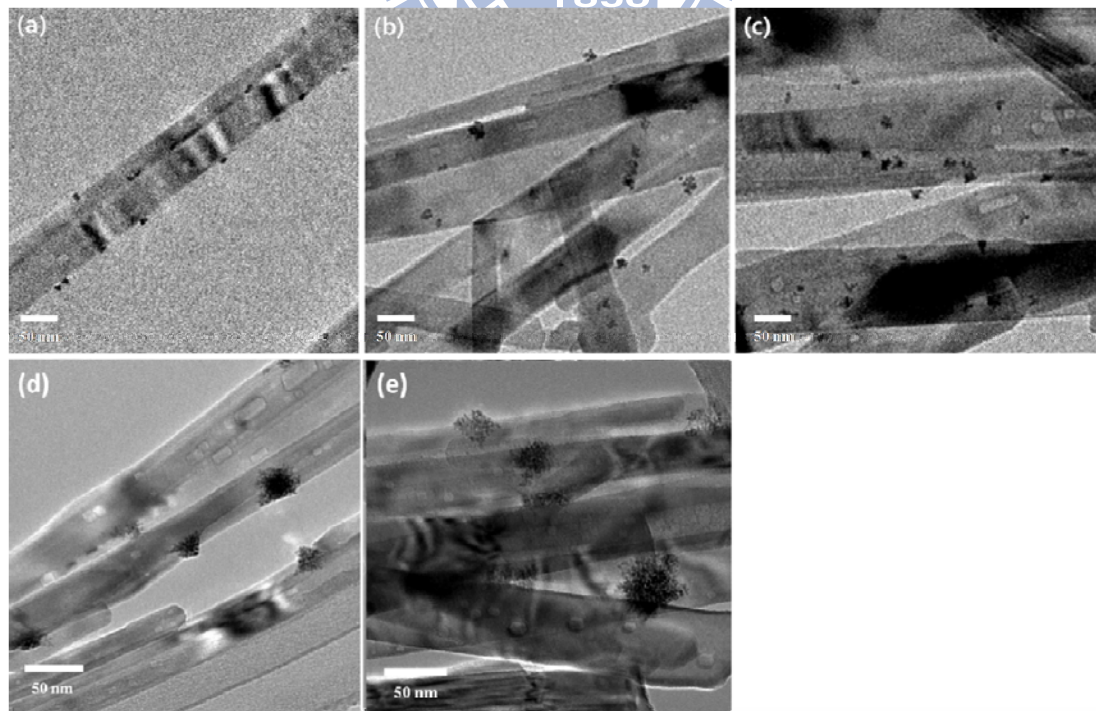


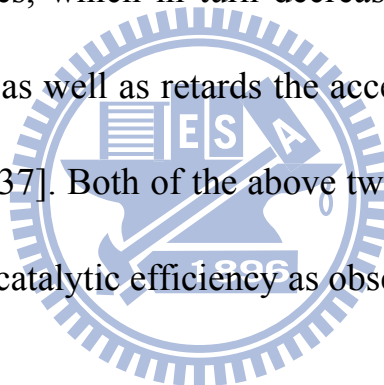
**Figure 3.2.2** TEM images of Pt-decorated TiO<sub>2</sub> NWs with the Pt contents of (a) 1.0, (b) 2.0, (c) 3.0, (d) 5.0 and (e) 10 wt %.

### 3.3 Photocatalytic Properties of Pt-decorated TiO<sub>2</sub> NWs

MB, a typical textile dye, was used as the model contaminant for photocatalysis here. Since MB is a cationic dye that may accept electrons from photocatalysts upon light illumination, we may realize the electron transfer event from TiO<sub>2</sub> to Pt for the present Pt-decorated TiO<sub>2</sub> NWs. Note that ethanol was used as the sacrificial holes scavenger for photocatalyst to facilitate the further utilization of photoexcited electrons. Figures 3.3.1 represents the time-dependended UV-Visible spectra of MB solutions under UV illumination in the presence of pristine TiO<sub>2</sub> NWs. It can be seen that the intensity of the characteristic absorption peak decreased with the irradiation time [36]. The bleaching of the absorption at 654 nm implies the reduction of MB and thus the operation of photocatalysis by using NWs. We then analyzed the normalized concentration of MB ( $C/C_0$ ) as a function of irradiation time in order to understand the progress of MB photodegradation (Figure 3.3.2). As compared to pure NWs, Pt-decorated samples exhibit superior photocatalytic efficiency toward MB photodegradation. This improvement mainly resulted from the deposited Pt that can promote charge separation by attracting the photoexcited electrons from NWs, thus providing more



electrons for the decomposition of MB. As increasing the amount of Pt from 1 to 3 wt%, an enhanced photocatalytic activity was found for TiO<sub>2</sub> NWs correspondingly. However, an obvious decrease in the photocatalytic activity was observed when Pt content was increased from 5 to 10 wt %. This outcome demonstrated an optimal content of Pt decoration for improving the photocatalytic performance of TiO<sub>2</sub> NWs. It has been widely documented that the excess content of metal may cover a large part of photocatalyst surfaces, which in turn decreases the number of active sites for photocatalysis as well as retards the access of light irradiation to photocatalyst surfaces [37]. Both of the above two situations may account for the depressed photocatalytic efficiency as observed here.



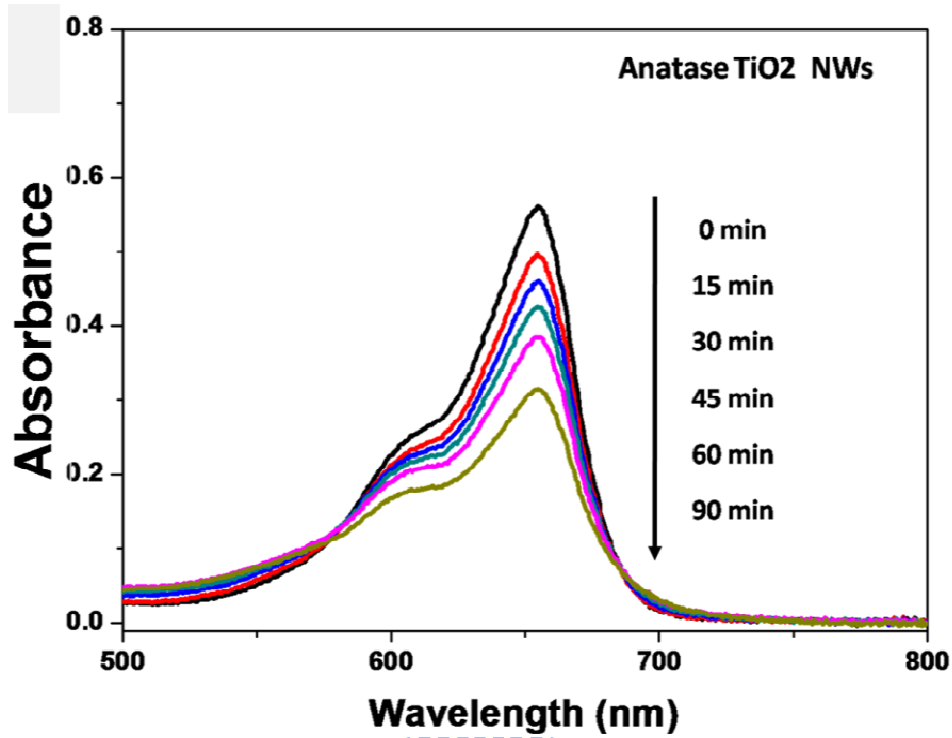


**Figure 3.3.1** Absorption spectra of MB solutions under different UV irradiation times by using TiO<sub>2</sub> NWs.

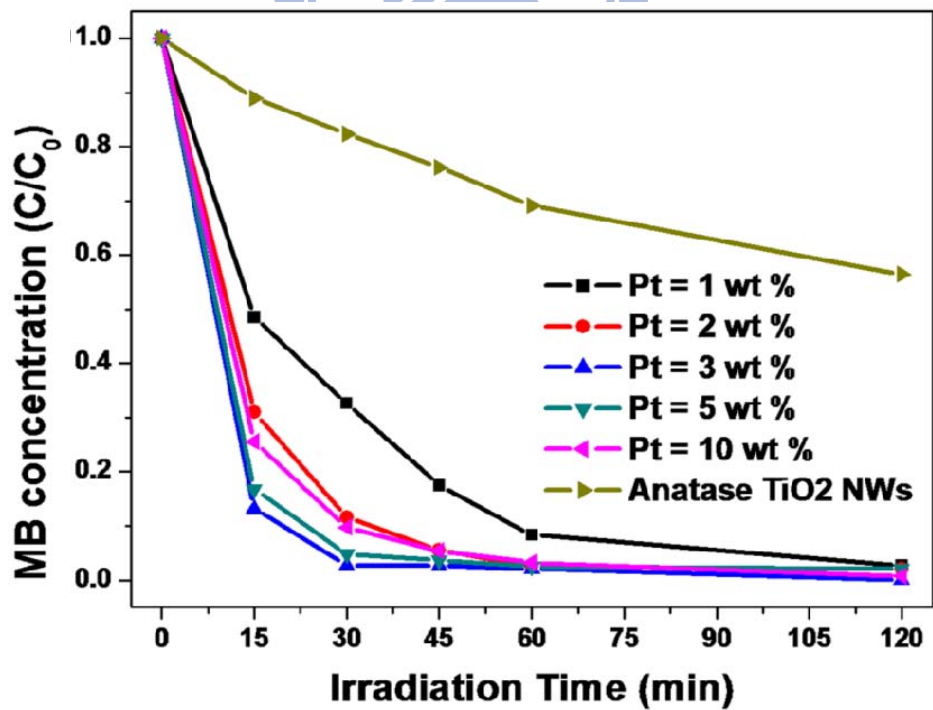


**Figure 3.3.2** C/C<sub>0</sub> versus irradiation time plots for MB photodegradation under UV illumination by using Pt-decorated TiO<sub>2</sub> NWs with various Pt contents.

### 3.4 Effects of Various Metal Decorations and Recycling Test

To further demonstrate the remarkable photocatalytic properties for the present Pt-decorated samples, five kinds of photocatalysts including Pt-loaded, Au-decorated, Ag-decorated, Pt-decorated TiO<sub>2</sub> NW, and P-25 TiO<sub>2</sub> powder were compared in MB photodegradation under the same conditions. Note that Pt-loaded sample was prepared by simply mixing NWs with Pt colloids, which led to the random distribution of Pt around TiO<sub>2</sub>. As to the preparation of Au- and Ag-decorated NWs, a similar approach to the synthesis of Pt-decorated sample was used. The comparative results were shown in Figure 3.4.1, from which several points can be observed. First, Pt-loaded sample did not perform as better as Pt-decorated NWs did, presumably owing to the less contact of Pt with NWs in Pt-loaded sample. Because of the limited contact between Pt and TiO<sub>2</sub> NWs, a retarded charge separation was expected for Pt-loaded NWs sample, thus leading to the lower photocatalytic activity. Second, as compared to the Ag- and Au-decorated samples, Pt-decorated NBs exhibited superior photocatalytic efficiency toward MB photodegradation, which can be explained by the difference of work function among the deposited metals. Among the three metals, Pt has the largest work

function [38], which means that the difference between the conduction band of  $\text{TiO}_2$  and the Fermi level of metal was the largest in Pt-decorated case. It had been pointed out that the driving force of electron transfer from semiconductor to metal is proportional to such energetic difference. In the current case, Pt-decorated  $\text{TiO}_2$  NWs may possess higher driving force for charge separation and consequently showed better photocatalytic efficiency as compared to Ag- and Au-decorated samples. Third, as compared to the commercial product like P-25  $\text{TiO}_2$  powder, Pt-decorated  $\text{TiO}_2$  NWs showed better photocatalytic performance, demonstrating their potential as an efficient photocatalyst in relevant redox reactions. We performed a recycling test by using Pt-decorated  $\text{TiO}_2$  NWs with the Pt content of 3 wt % to investigate their recyclability and stability. As shown in Figure 3.4.2, no obvious decay of photocatalytic efficiency was found for Pt-decorated NWs after being repeatedly used for three times in MB photodegradation. This result shows that the present Pt-decorated  $\text{TiO}_2$  NWs had excellent stability and could be promisingly utilized in the long-term course of photocatalysis.

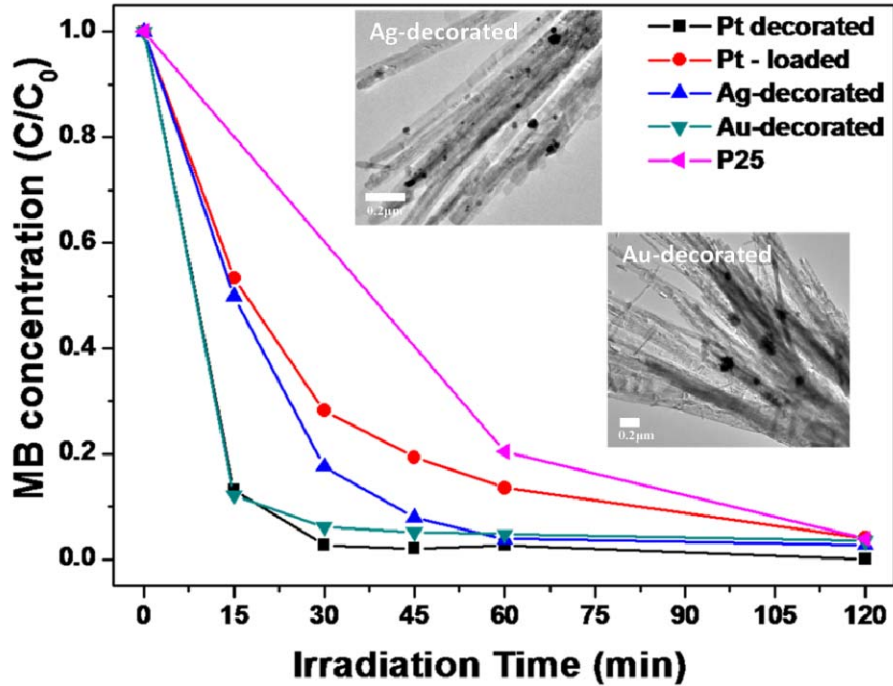


**Figure 3.4.1** The MB photodegradation results by using different photocatalysts including Pt-loaded, Pt-decorated, Ag-decorated, Au-decorated TiO<sub>2</sub> NWs, and P-25 TiO<sub>2</sub> powder. Content of metal = 3.0 wt %. The insets were the corresponding TEM images.

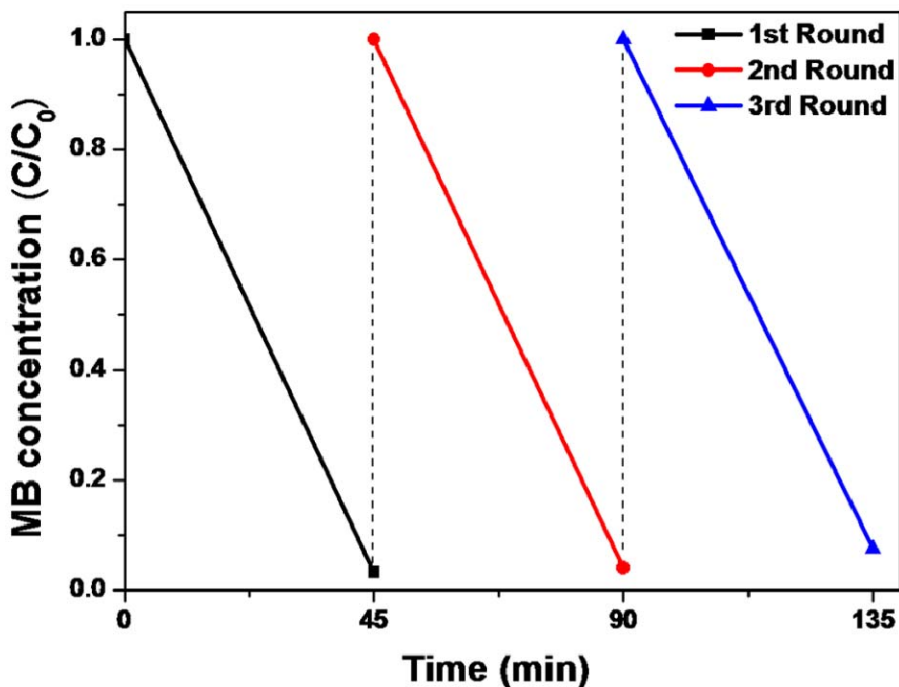


**Figure 3.4.2** Recycling test on Pt-decorated TiO<sub>2</sub> NWs with Pt content of 3 wt %.

### 3.5 Decoration of In<sub>2</sub>O<sub>3</sub> on TiO<sub>2</sub> NWs

On the other hand, we may provide TiO<sub>2</sub> NWs with an appropriate hole-acceptor to scavenge the photogenerated holes of TiO<sub>2</sub> for photocatalytic oxidation purpose. Through a precipitation-annealing process, we could decorate TiO<sub>2</sub> NWs with In<sub>2</sub>O<sub>3</sub> nanoparticles which had suitable band structures to allow hole transfer from TiO<sub>2</sub> to In<sub>2</sub>O<sub>3</sub> ( $E_{cb} = -0.62\text{V}$ ,  $E_{vb} = 2.18\text{V}$  vs. NHE for In<sub>2</sub>O<sub>3</sub>;  $E_{cb} = -0.29\text{V}$ ,  $E_{vb} = 2.91\text{V}$  vs. NHE for anatase TiO<sub>2</sub>) [39]. As shown in Figure 3.5.1 (a), the diameter of In<sub>2</sub>O<sub>3</sub> nanoparticles grown at the surfaces of TiO<sub>2</sub> NWs was about 20~50 nm. The corresponding XRD analysis shown in Figure 3.5.1 (c) confirmed the crystal structure of In<sub>2</sub>O<sub>3</sub> nanoparticles. Note that pure In<sub>2</sub>O<sub>3</sub> nanoparticles can also be obtained by using the same procedure without the addition of NWs. Figure 3.5.1 (b) displays the morphology of the single-phase In<sub>2</sub>O<sub>3</sub> nanoparticles. The dimension and shape of the pure In<sub>2</sub>O<sub>3</sub> nanoparticles were similar to those deposited at the surfaces of NWs, with which we may make a fair comparison of their photocatalytic properties.

The decoration of TiO<sub>2</sub> NWs with In<sub>2</sub>O<sub>3</sub> nanoparticles was achieved through a precipitation-annealing process. Upon mixing InCl<sub>3</sub> with

NH<sub>4</sub>OH solution, white precipitation of an abundant amount rapidly formed within the solution. The corresponding XRD analysis show that the precipitated particles were made of In(OH)<sub>3</sub>, which resulted from the reaction of InCl<sub>3</sub> with NH<sub>4</sub>OH. Subsequently, TiO<sub>2</sub> NWs of a given amount were added into the above solution and the mixed solution was stirred for 12 h to allow the attachment of In(OH)<sub>3</sub> nanoparticles onto the surfaces of TiO<sub>2</sub> NWs. SEM investigation shown in Figure 3.5.2 clearly reveals the decoration of NWs with a lot of nanoparticles of In(OH)<sub>3</sub>. During the stirring process, it was expected that In–OH bonds of In(OH)<sub>3</sub> nanoparticles would bind to the unsaturated oxygen at TiO<sub>2</sub> surfaces to form Ti–O–In–OH linkage, which further led to the attachment of In(OH)<sub>3</sub> onto TiO<sub>2</sub> NWs [40]. These In(OH)<sub>3</sub>-decorated NWs were then annealed at 700<sup>o</sup>C in air for 2 h to transform In(OH)<sub>3</sub> into In<sub>2</sub>O<sub>3</sub> through a dehydration process. As a result, In<sub>2</sub>O<sub>3</sub>-decorated TiO<sub>2</sub> NWs were obtained. The HRTEM image taken at the interface of NW and nanoparticle regions of In<sub>2</sub>O<sub>3</sub>-TiO<sub>2</sub> NWs clearly reveals two distinct sets of lattice fringes (Figure 3.5.3). An interlayer spacing of 0.18 nm was observed in the NW region, in good agreement with the *d* spacing of the (200) lattice planes of TiO<sub>2</sub> [28]. In the particle region, interlayer spacings

of 0.29 nm and 0.41 nm were obtained, complying with the lattice spacing of (222) and (211) planes of the bcc  $\text{In}_2\text{O}_3$ , respectively [41]. Figure 3.5.4 reveals the gradual increase in  $\text{In}_2\text{O}_3$  particle density for  $\text{In}_2\text{O}_3$ -decorated  $\text{TiO}_2$  NWs, which was achieved by employing  $\text{InCl}_3$  of increasing amounts. As increasing the amount of  $\text{InCl}_3$ , the resultant surface-attached  $\text{In}_2\text{O}_3$  particles became prevalent and aggregated on NW surfaces.

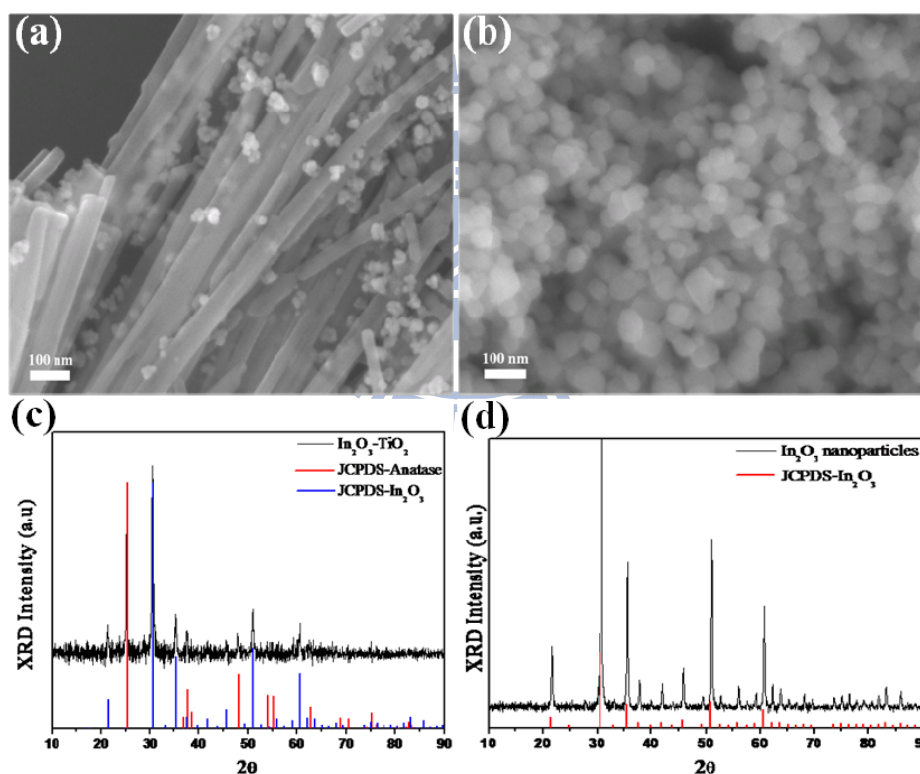


**Figure 3.5.1** SEM images of (a)  $\text{In}_2\text{O}_3$ -decorated  $\text{TiO}_2$  NWs (molar ratio of  $\text{In}_2\text{O}_3$  to  $\text{TiO}_2 = 1:1$ ), and (b) pure  $\text{In}_2\text{O}_3$  nanoparticles. The corresponding XRD patterns were shown in (c) and (d).



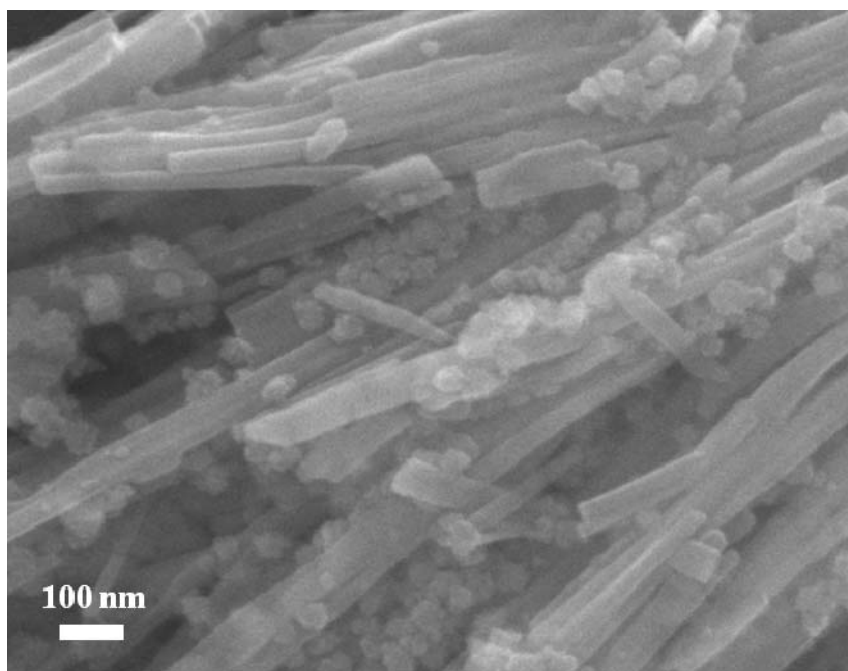


**Figure 3.5.2** SEM image of  $\text{In}(\text{OH})_3$ -decorated  $\text{TiO}_2$  NWs.

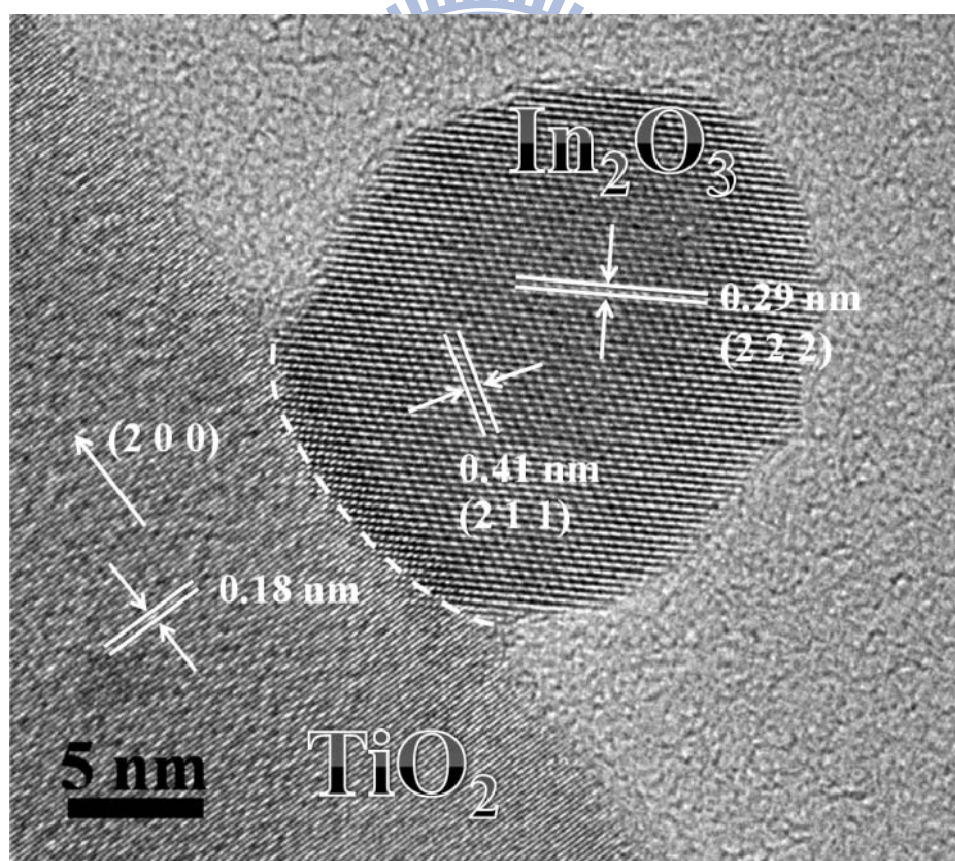


**Figure 3.5.3** HRTEM image taken on an individual  $\text{In}_2\text{O}_3$ -decorated  $\text{TiO}_2$  NW. The interface between  $\text{TiO}_2$  and  $\text{In}_2\text{O}_3$  was highlighted with a dashed line.

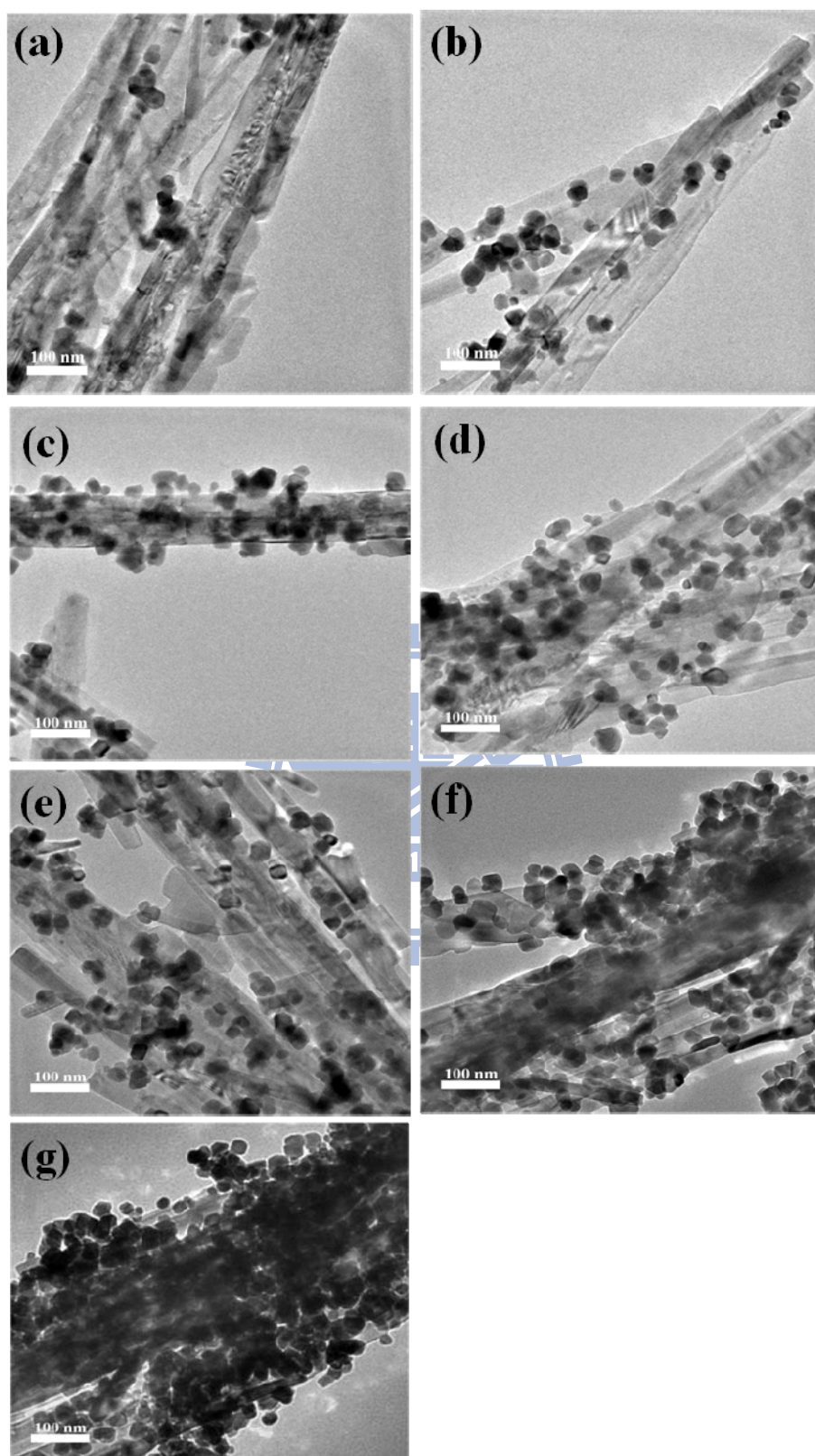


**Figure 3.5.4**  $\text{In}_2\text{O}_3$ -decorated  $\text{TiO}_2$  NWs with various  $\text{In}_2\text{O}_3/\text{TiO}_2$  molar ratios of (a) 0.25:1, (b) 0.5:1, (c) 1:1, (d) 1.5:1, (e) 2:1, (f) 2.5:1 (g) 5:1

### 3.6 Photocatalytic Properties of In<sub>2</sub>O<sub>3</sub>-decorated TiO<sub>2</sub> NWs

To investigate the photocatalytic properties of In<sub>2</sub>O<sub>3</sub>-decorated TiO<sub>2</sub> NWs, RB was used as the test pollutant since it could react with photogenerated holes to get decomposed through a photocatalytic oxidation process. Note that the oxygen dissolved in water may act as the sacrificial electron consumer for photocatalyst to facilitate the further utilization of photogenerated holes. The time-dependent UV-visible spectra of RB solutions under UV illumination in the presence of TiO<sub>2</sub> NWs were first shown in Figure 3.6.1. It can be seen that the intensity of the characteristic absorption peak at 554 nm [42] decreased dramatically with the irradiation time, implying the successful degradation of RB by the photocatalysis of TiO<sub>2</sub>. Figure 3.6.2 displays the photodegradation results by using In<sub>2</sub>O<sub>3</sub>-decorated TiO<sub>2</sub> NWs with different In<sub>2</sub>O<sub>3</sub>/TiO<sub>2</sub> molar ratios. The photocatalytic efficiency of TiO<sub>2</sub> NWs was enhanced as increasing the molar ratio of In<sub>2</sub>O<sub>3</sub>/TiO<sub>2</sub> from 0.25 to 1.0. This enhancement mainly came from the deposited In<sub>2</sub>O<sub>3</sub> that can promote charge separation by attracting more photogenerated holes from TiO<sub>2</sub> NWs, thus providing more holes for the decomposition of RB. When the molar ratio of In<sub>2</sub>O<sub>3</sub>/TiO<sub>2</sub> was further increased to 2.5 and 5.0, a decrease in the

photocatalytic activity was however observed for TiO<sub>2</sub> NWs. This depression might result from the excess In<sub>2</sub>O<sub>3</sub> nanoparticles which may cover a large part of NW surfaces to block the light absorption of TiO<sub>2</sub> [43]. As a result, an unfavorable effect, analogous to that of excess metal loading, would emerge to hinder the resulting photocatalytic performance of TiO<sub>2</sub>. Although In<sub>2</sub>O<sub>3</sub> itself may still absorb light to generate charge carriers, the efficiency for these charge carriers to participate in photocatalysis was actually poor, as can be clearly seen in Figure 3.6.2.

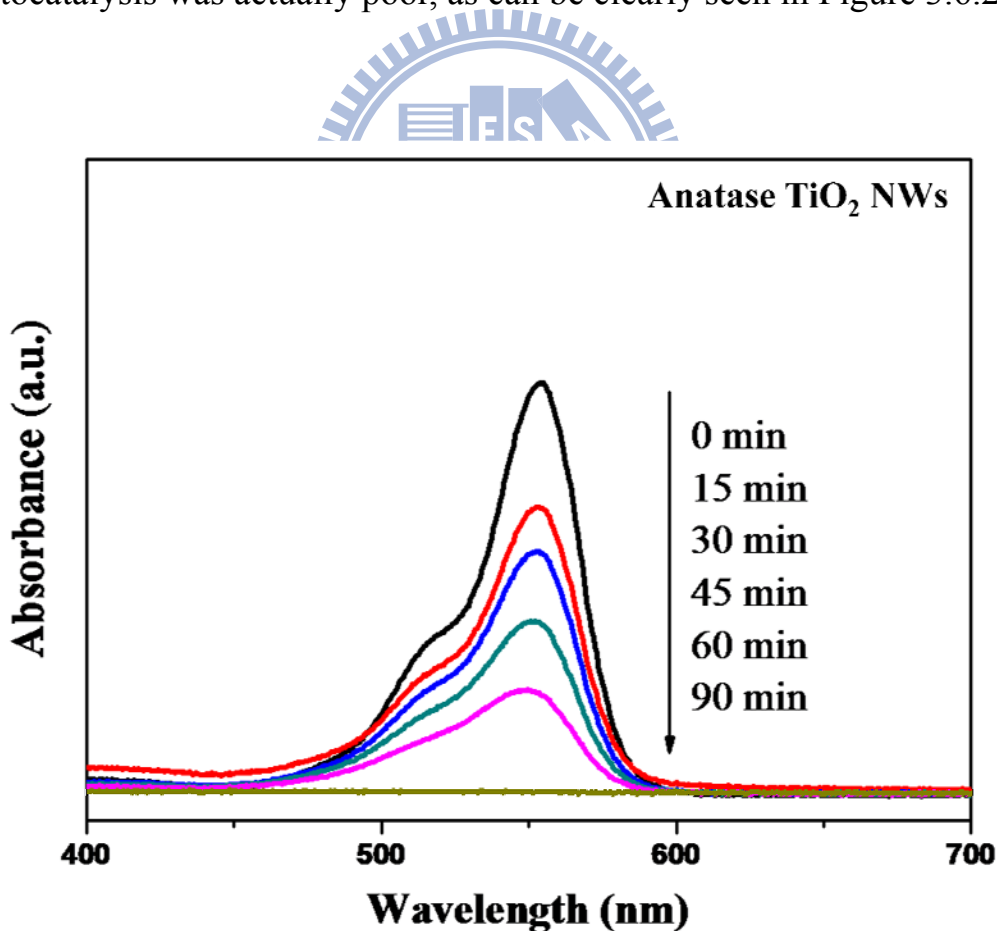


**Figure 3.6.1** Absorption spectra of RB solutions under different UV irradiation times by using TiO<sub>2</sub> NWs.

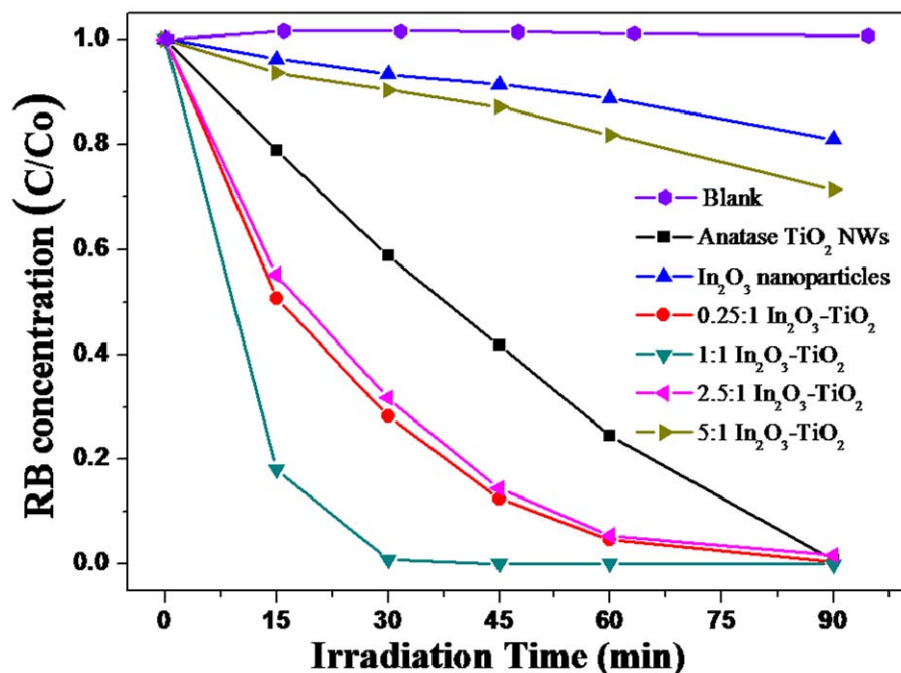


**Figure 3.6.2**  $C/C_0$  versus irradiation time plots for RB photodegradation under UV illumination by using  $\text{In}_2\text{O}_3$ -decorated  $\text{TiO}_2$  NWs with various  $\text{In}_2\text{O}_3/\text{TiO}_2$  molar ratios. The results by using pure  $\text{TiO}_2$  NWs and pure  $\text{In}_2\text{O}_3$  nanoparticles were also included for comparison.

To demonstrate the remarkable photocatalytic properties for  $\text{In}_2\text{O}_3$ -decorated  $\text{TiO}_2$  NWs, further comparative experiments were conducted. In Figure 3.6.3, three different photocatalysts including  $\text{In}_2\text{O}_3$ -loaded,  $\text{In}_2\text{O}_3$ -decorated  $\text{TiO}_2$  NWs, and P-25  $\text{TiO}_2$  powder were used and compared. Note that  $\text{In}_2\text{O}_3$ -loaded NWs were prepared by simply mixing NWs with  $\text{In}_2\text{O}_3$  nanoparticles, resulting in a random distribution of  $\text{In}_2\text{O}_3$  nanoparticles around NWs. The as-prepared  $\text{In}_2\text{O}_3$ -decorated NWs exhibited superior photocatalytic performance as compared to the other two samples. This is due to the pronounced charge separation which was

believed to occur at the interface of  $\text{In}_2\text{O}_3/\text{TiO}_2$  in  $\text{In}_2\text{O}_3$ -decorated  $\text{TiO}_2$  NWs. Furthermore, these  $\text{In}_2\text{O}_3$ -decorated NWs were used in the recycling photocatalytic operation to test their recyclability and stability. As shown in Figure 3.6.4, after being repeatedly used for three times in RB photodegradation, no obvious decay of photocatalytic efficiency was observed. This result demonstrates that the present  $\text{In}_2\text{O}_3$ -decorated  $\text{TiO}_2$  NWs could be promisingly utilized in the long-term course of photocatalysis.

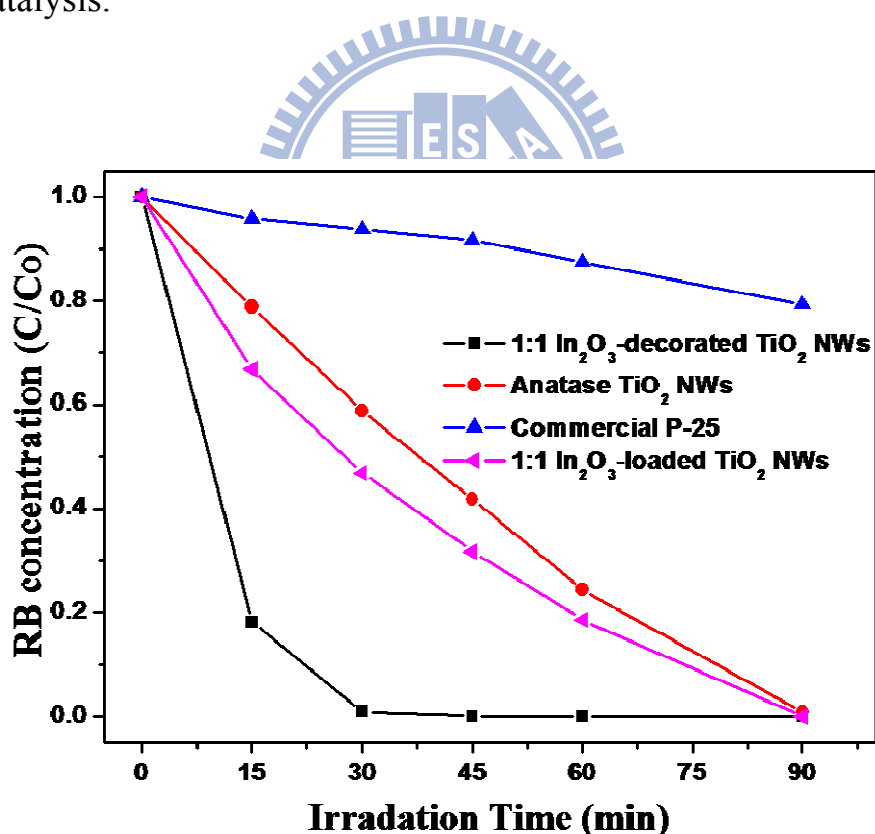


**Figure 3.6.3** The RB photodegradation results under UV light irradiation by using different photocatalysts including  $\text{In}_2\text{O}_3$ -loaded,  $\text{In}_2\text{O}_3$ -decorated,  $\text{TiO}_2$  NWs and commercial P-25  $\text{TiO}_2$  powders. Molar ratio of  $\text{In}_2\text{O}_3/\text{TiO}_2$  is 1:1.

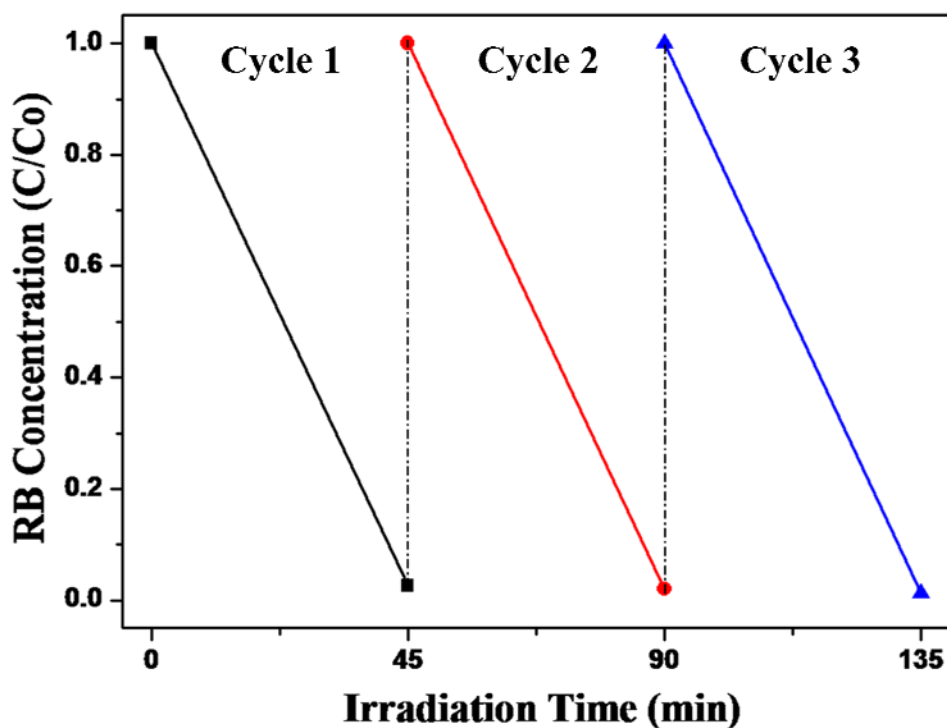
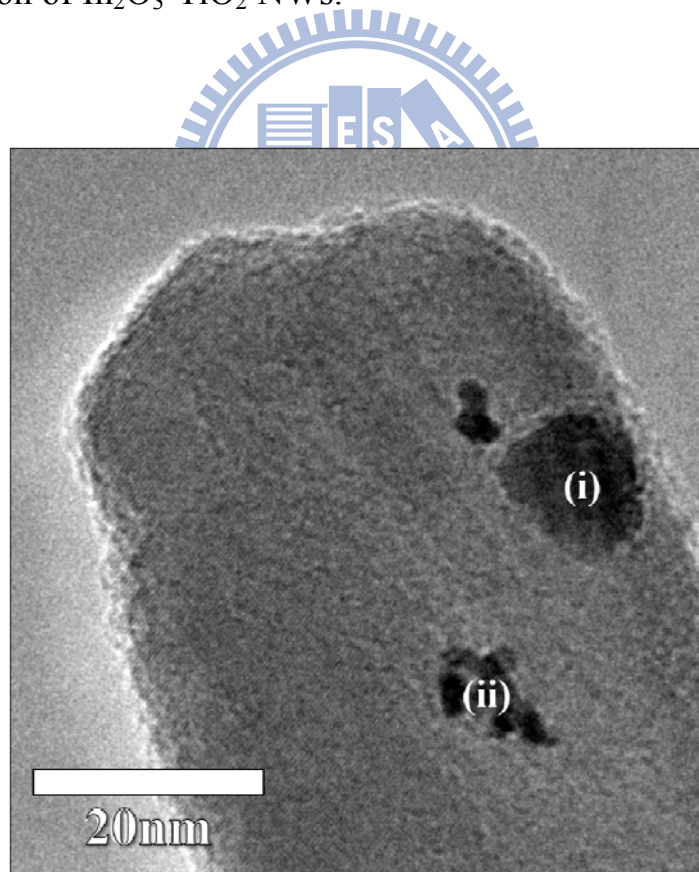


**Figure 3.6.4** Recycling test on  $\text{In}_2\text{O}_3$ -decorated  $\text{TiO}_2$  NWs with the  $\text{In}_2\text{O}_3/\text{TiO}_2$  molar ratio of 1:1.

### 3.7 Further Decoration of Pt on $\text{In}_2\text{O}_3$ - $\text{TiO}_2$ NWs

To further promote the photocatalytic efficiency of  $\text{TiO}_2$ , we applied both Pt and  $\text{In}_2\text{O}_3$  decorations for  $\text{TiO}_2$  NWs. Due to the difference in band structures between  $\text{In}_2\text{O}_3$  and  $\text{TiO}_2$ , the photogenerated holes in  $\text{TiO}_2$  would preferentially transfer to  $\text{In}_2\text{O}_3$ , leaving photoexcited electrons in  $\text{TiO}_2$  domain to achieve charge separation. We can then utilize this characteristic to deposit Pt at the  $\text{TiO}_2$  region of  $\text{In}_2\text{O}_3$ - $\text{TiO}_2$  NWs by using the photodeposition method described in section 3.2. Figure 3.7.1 displays the TEM images of  $\text{In}_2\text{O}_3$ -decorated  $\text{TiO}_2$  NWs after they were

treated with the Pt photodeposition process. The TEM-EDS results shown in Figure 3.7.1 clearly reveal the deposition of Pt nanoparticles at TiO<sub>2</sub> region of In<sub>2</sub>O<sub>3</sub>-TiO<sub>2</sub> NWs. This outcome reaffirms our proposition that In<sub>2</sub>O<sub>3</sub> can attract photogenerated holes of TiO<sub>2</sub> to leave photoexcited electrons in TiO<sub>2</sub>. Upon UV light irradiation, the photoexcited electrons in TiO<sub>2</sub> region of In<sub>2</sub>O<sub>3</sub>-TiO<sub>2</sub> NWs can then react with the surrounding PtCl<sub>6</sub><sup>2-</sup> ions to grow Pt nanoparticles, resulting in the deposition of Pt at the TiO<sub>2</sub> region of In<sub>2</sub>O<sub>3</sub>-TiO<sub>2</sub> NWs.





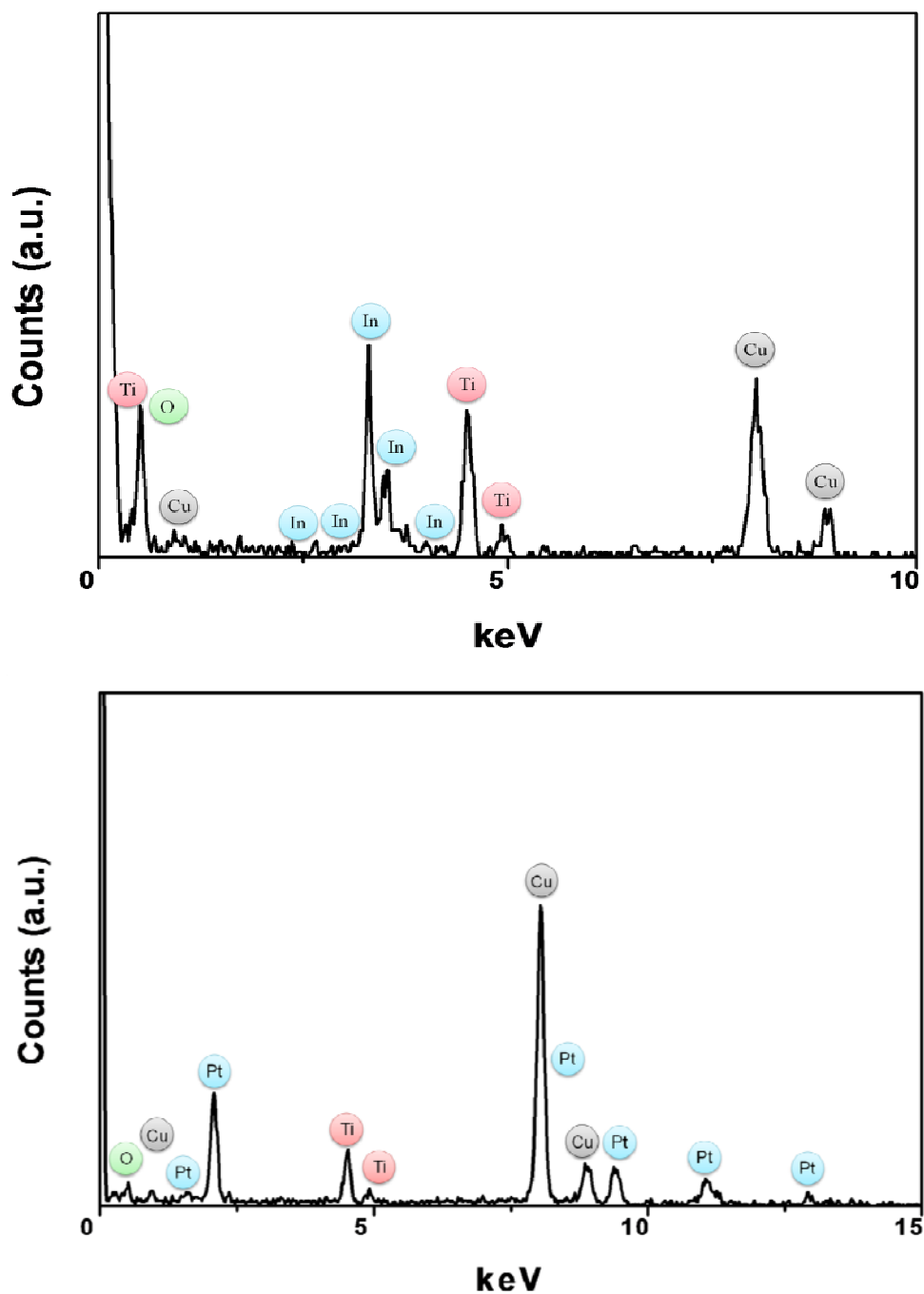
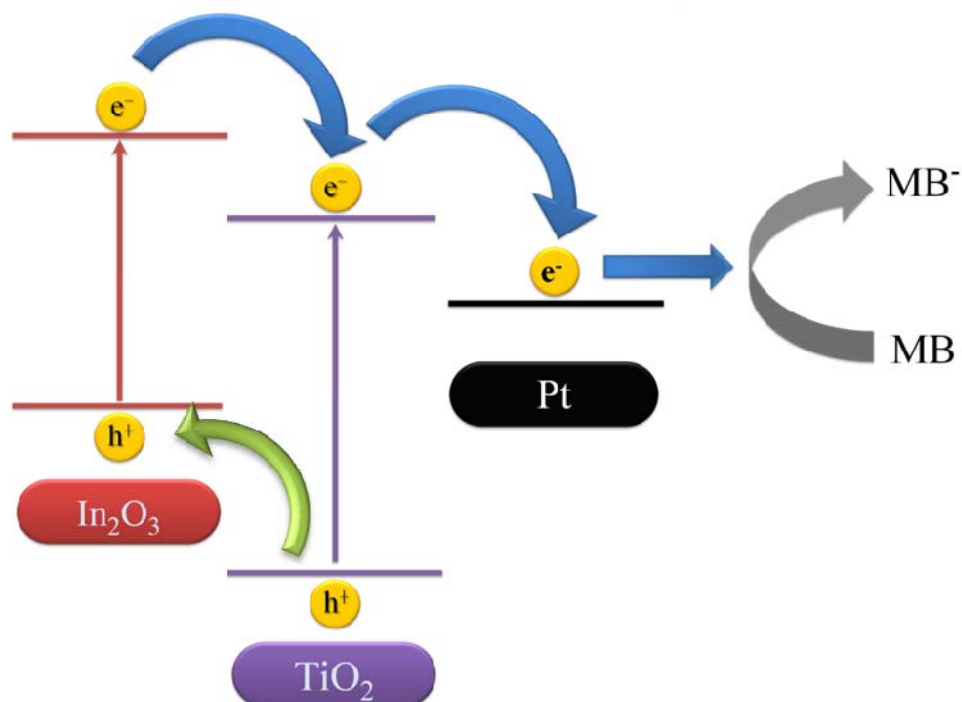


**Figure 3.7.1** TEM image and the corresponding EDS spectra for  $\text{In}_2\text{O}_3\text{-TiO}_2\text{-Pt}$  NWs.

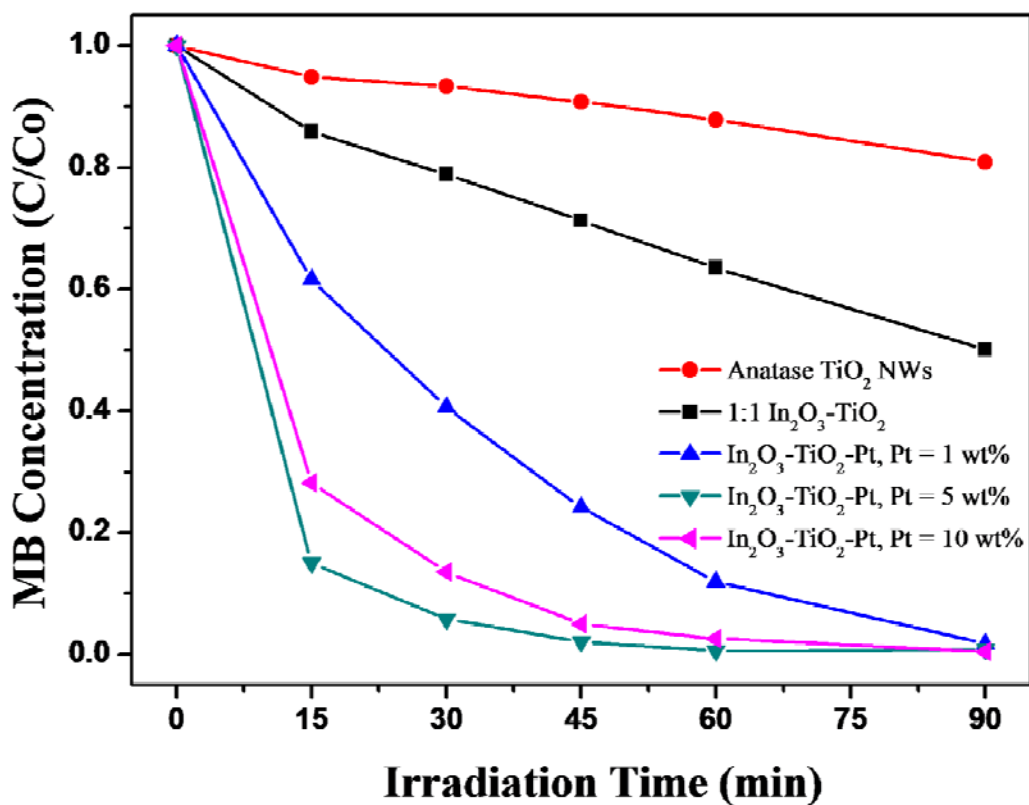
### 3.8 Photocatalytic Properties of $\text{In}_2\text{O}_3\text{-TiO}_2\text{-Pt}$ NWs

To demonstrate the even superior photocatalytic performance for  $\text{In}_2\text{O}_3\text{-TiO}_2\text{-Pt}$  NWs, MB which can serve as an electron-acceptor was

again used as the test pollutant here. The band structures shown in Figure 3.8.1 illustrate the charge transfer event that occurred in  $\text{In}_2\text{O}_3\text{-TiO}_2\text{-Pt}$  NWs and the subsequent photocatalysis to decompose MB. We expected that much more photoexcited electrons can be extracted from  $\text{In}_2\text{O}_3\text{-TiO}_2\text{-Pt}$  NWs, which may further lead to the enhanced photocatalytic efficiency toward MB photodegradation. As shown in Figure 3.8.2, an even better performance of photocatalysis was observed for  $\text{In}_2\text{O}_3\text{-TiO}_2$  NWs once they were decorated with Pt. There again existed an optimal content of Pt (5.0 wt% here) for improving the photocatalytic efficiency of  $\text{In}_2\text{O}_3\text{-TiO}_2$  NWs. Above this optimal value, the photocatalytic efficiency of NWs was depressed due to the excess coverage of Pt on  $\text{TiO}_2$  surfaces.

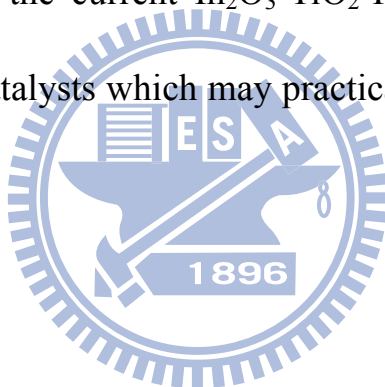


**Figure 3.8.1** Band structures and charge transfer event in  $\text{In}_2\text{O}_3$ - $\text{TiO}_2$ -Pt NWs.



**Figure 3.8.2** The MB photodegradation results under UV light irradiation by using  $\text{In}_2\text{O}_3$ - $\text{TiO}_2$ -Pt NWs with various Pt contents.

Since  $\text{In}_2\text{O}_3$  has a direct bandgap energy of 2.8 eV, the current  $\text{In}_2\text{O}_3$ - $\text{TiO}_2$ -Pt NWs may be sensitized by  $\text{In}_2\text{O}_3$  to absorb visible light and perform photocatalysis. To explore the applicability of these NWs under visible light illumination, their photocatalytic performance under natural sunlight was evaluated. As illustrated in Figure 3.8.3, after exposure to 1 h of daytime sunlight, MB was totally degraded by using  $\text{In}_2\text{O}_3$ - $\text{TiO}_2$ -Pt NWs, accompanied with an obvious decoloration of the resultant solution. This result shows that the current  $\text{In}_2\text{O}_3$ - $\text{TiO}_2$ -Pt NWs can be used as highly efficient photocatalysts which may practically harvest energy from sunlight.



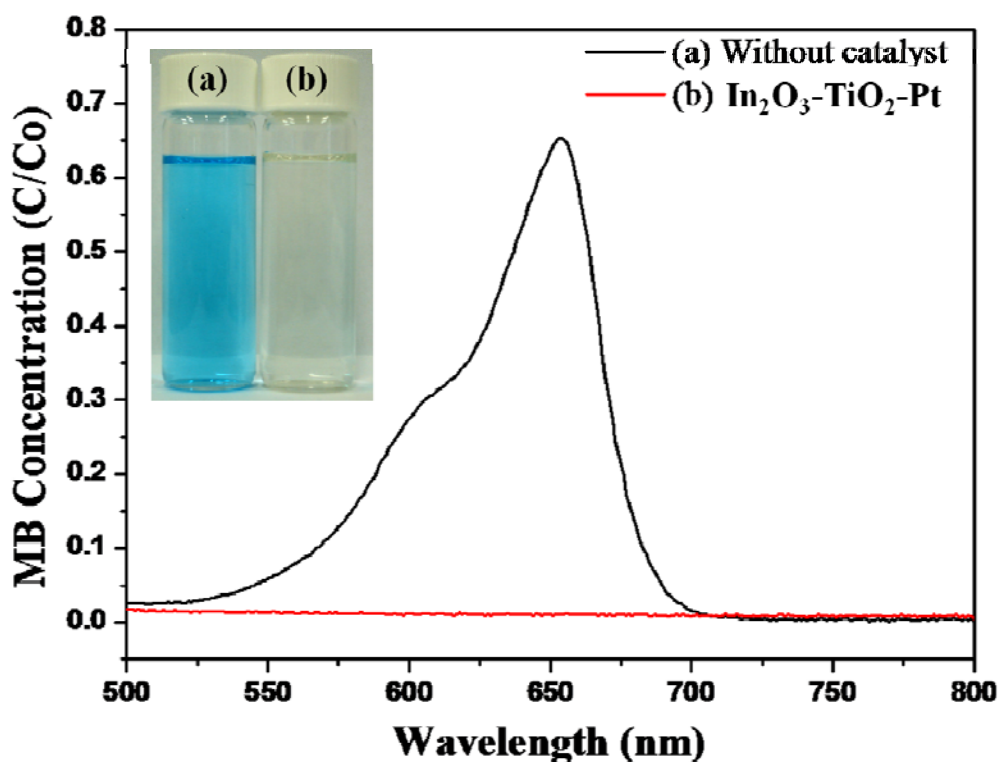


**Figure 3.8.3** Absorption spectra of MB solutions after exposure of 1 h of daytime sunlight (a) without any catalyst and (b) in the presence of  $\text{In}_2\text{O}_3\text{-TiO}_2\text{-Pt}$  NWs. Content of Pt = 5.0 wt %. Insets show the corresponding solution color.

### 3.9 Photocurrent Measurement for $\text{In}_2\text{O}_3\text{-TiO}_2\text{-Pt}$ NWs

To further elucidate the effect of Pt on the charge separation of  $\text{In}_2\text{O}_3$ -decorated  $\text{TiO}_2$  NWs, we compared the photocurrent response of pure  $\text{TiO}_2$  NW,  $\text{In}_2\text{O}_3\text{-TiO}_2$  NW, and  $\text{In}_2\text{O}_3\text{-TiO}_2\text{-Pt}$  NW electrodes by inserting them in a photoelectrochemical cell. Figure 3.9.1 depicts the photocurrent generation for the three kinds of NW electrodes subjected to the white light irradiation. There were several points to be observed from the figure. First, all the electrodes showed prompt response to the on/off

cycles of light illumination, demonstrating the effective charge transfer and successful electron collection for the samples within the photoelectrochemical cell. Second, the photocurrent of TiO<sub>2</sub> NWs was significantly enhanced if they were decorated with In<sub>2</sub>O<sub>3</sub>. The significant retardation of charge recombination in In<sub>2</sub>O<sub>3</sub>-TiO<sub>2</sub> NWs accounted for such a drastic photocurrent enhancement [44]. Third, a much higher photocurrent was produced when In<sub>2</sub>O<sub>3</sub>-TiO<sub>2</sub> NWs were further decorated with Pt of 1.0 wt%. This outcome arose from the increasing driving force of electron transfer from In<sub>2</sub>O<sub>3</sub> to TiO<sub>2</sub> achieved by the decoration of Pt on TiO<sub>2</sub> surfaces. Note that semiconductor-metal heterostructures would undergo a Fermi level equilibration due to the accumulation of photexcited electrons in metal [45]. The equilibrated Fermi level of such composite system appeared to be lower in potential (less negative) than that of the corresponding pure semiconductor. As illustrated in Figure 3.9.2, the apparent Fermi level of TiO<sub>2</sub> in In<sub>2</sub>O<sub>3</sub>-TiO<sub>2</sub>-Pt NWs ( $E_F^{**}$ ) was presumably lower in potential than that of TiO<sub>2</sub> in In<sub>2</sub>O<sub>3</sub>-TiO<sub>2</sub> NWs ( $E_F^*$ ). A larger energetic difference in Fermi levels between In<sub>2</sub>O<sub>3</sub> and TiO<sub>2</sub> was thus expected for In<sub>2</sub>O<sub>3</sub>-TiO<sub>2</sub>-Pt NW system, which in turn promote the driving force of electron transfer from In<sub>2</sub>O<sub>3</sub> to TiO<sub>2</sub> domains. As a result,

an enhancement in the resulting photocurrent production was observed for  $\text{In}_2\text{O}_3\text{-TiO}_2\text{-Pt}$  NWs. The photocurrent generated from  $\text{In}_2\text{O}_3\text{-TiO}_2\text{-Pt}$  NWs was however depressed as the content of Pt was increased to 5.0 and 10 wt%. We supposed that too much Pt deposited on  $\text{TiO}_2$  of  $\text{In}_2\text{O}_3\text{-TiO}_2$  NWs would trap the photoexcited electrons in a considerably high amount, thus leading to a decreased number of electrons that were collected by the external voltmeter.

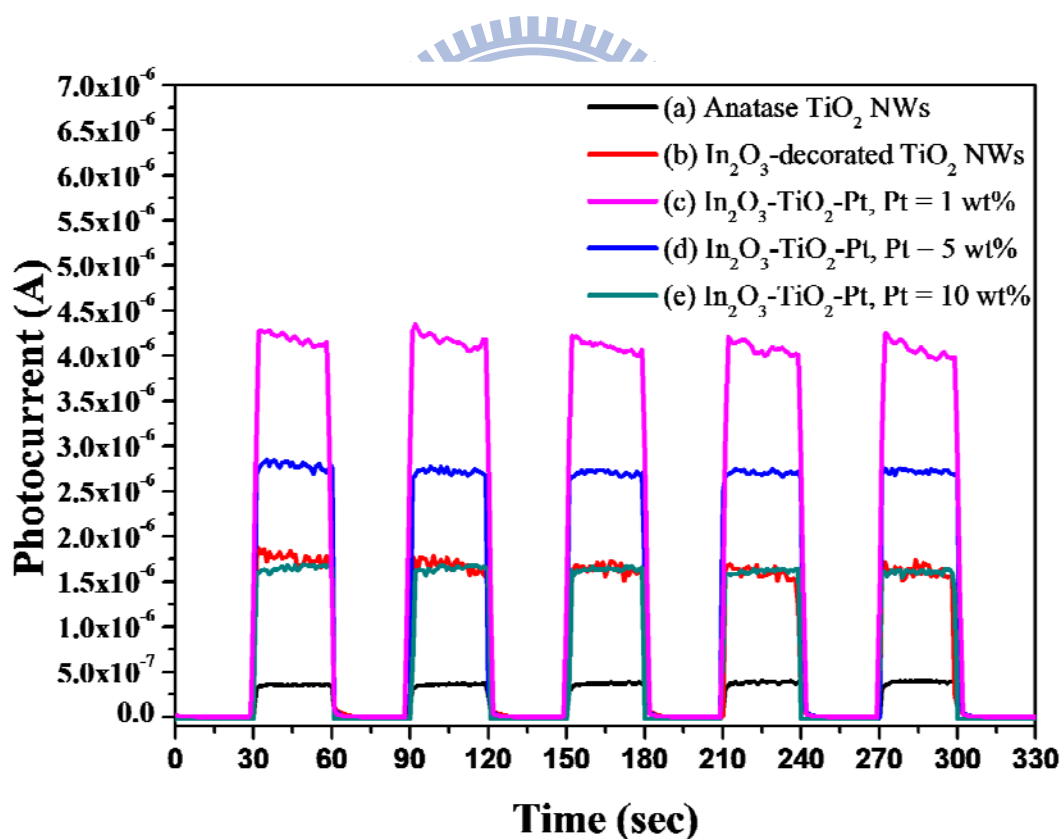


**Figure 3.9.1** Photocurrent response of pure  $\text{TiO}_2$  NWs,  $\text{In}_2\text{O}_3\text{-TiO}_2$  NWs and  $\text{In}_2\text{O}_3\text{-TiO}_2\text{-Pt}$  NWs with different Pt contents.

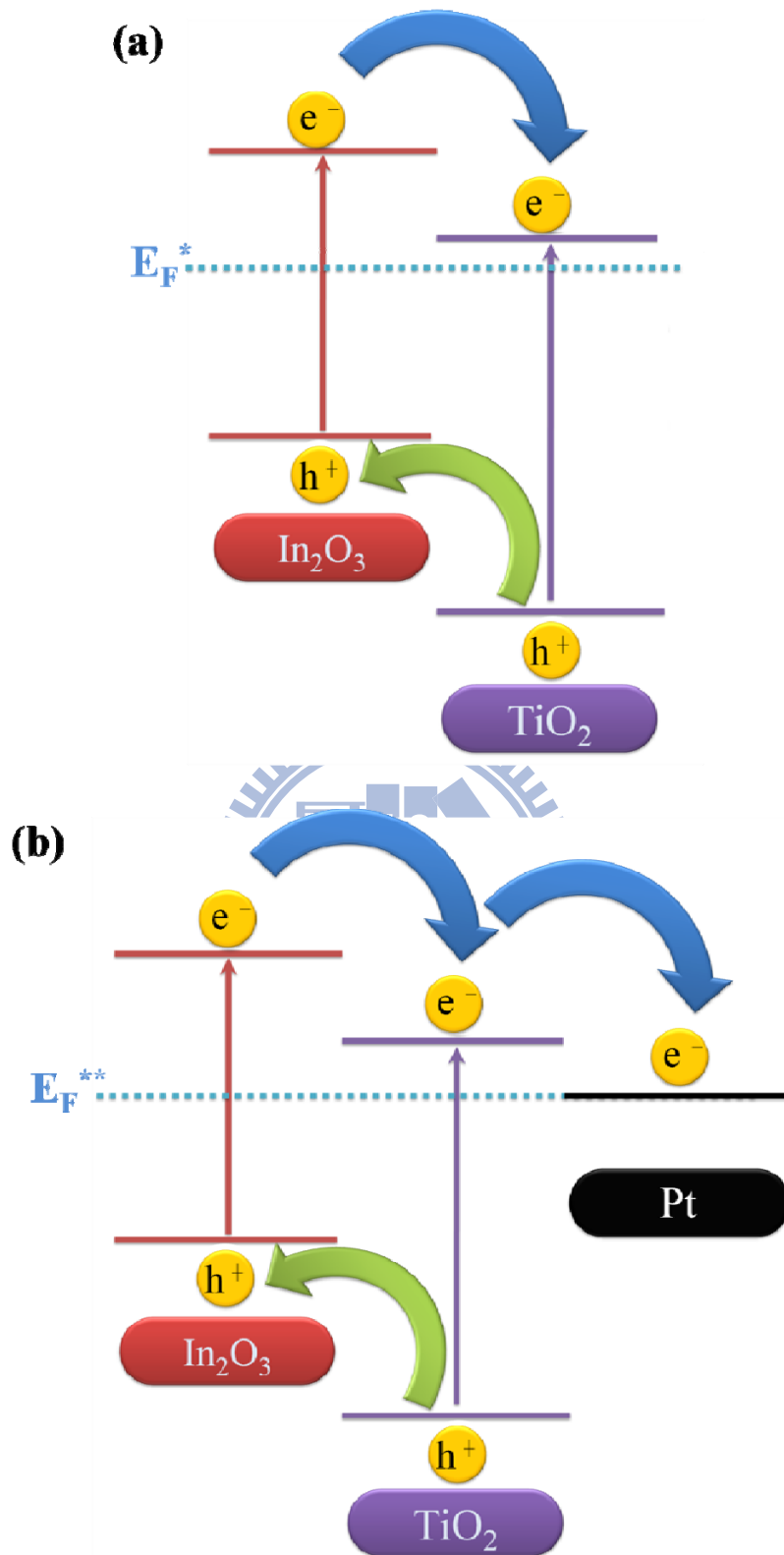
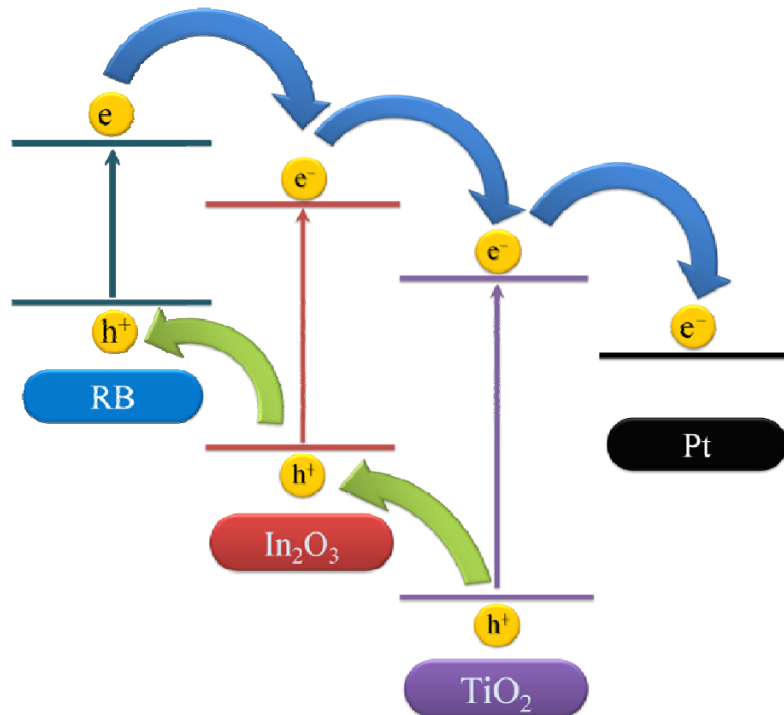


**Figure 3.9.2** Illustration of the apparent Fermi level potential of TiO<sub>2</sub> in (a) In<sub>2</sub>O<sub>3</sub>-TiO<sub>2</sub> and (b) In<sub>2</sub>O<sub>3</sub>-TiO<sub>2</sub>-Pt systems.

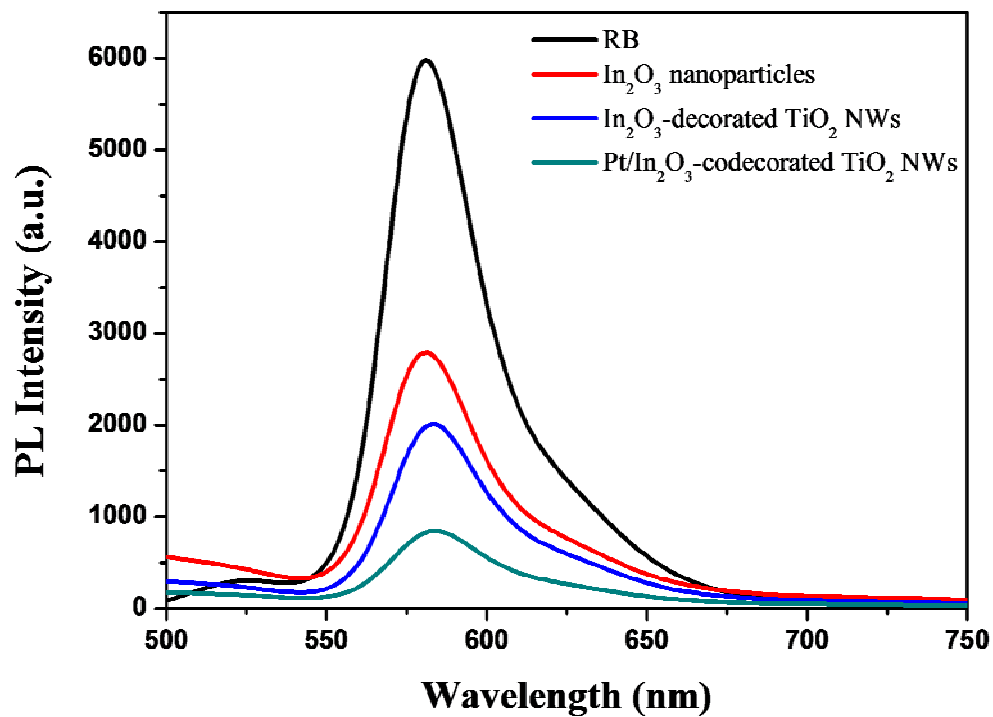


### 3.10 Time-Resolved Photoluminescence Spectra

If the observed photocurrent enhancement with the decoration of Pt (1.0 wt%) on  $\text{In}_2\text{O}_3\text{-TiO}_2$  NWs indeed involved the increasing driving force of electron transfer from  $\text{In}_2\text{O}_3$  to  $\text{TiO}_2$ , we should be able to reveal this event in the corresponding emission decay profiles. Since RB has the band structure that can well fit to  $\text{In}_2\text{O}_3$  to allow charge transfer, it was used as the sensitizer to monitor the charge transfer event among  $\text{In}_2\text{O}_3$ ,  $\text{TiO}_2$  and Pt (Figure 3.10.1). As shown in Figure 3.10.2, a significant quenching in the PL emission of RB was observed for  $\text{In}_2\text{O}_3$  as compared to pure RB. Such quenching became more noticeable in  $\text{In}_2\text{O}_3\text{-TiO}_2$  and even more significant in  $\text{In}_2\text{O}_3\text{-TiO}_2\text{-Pt}$  sample, implying the successful electron transfer from RB to  $\text{In}_2\text{O}_3$ , then  $\text{TiO}_2$  and finally Pt.



**Figure 3.10.1** Charge separation scheme for Pt/In<sub>2</sub>O<sub>3</sub>/TiO<sub>2</sub> in present of RB dye.



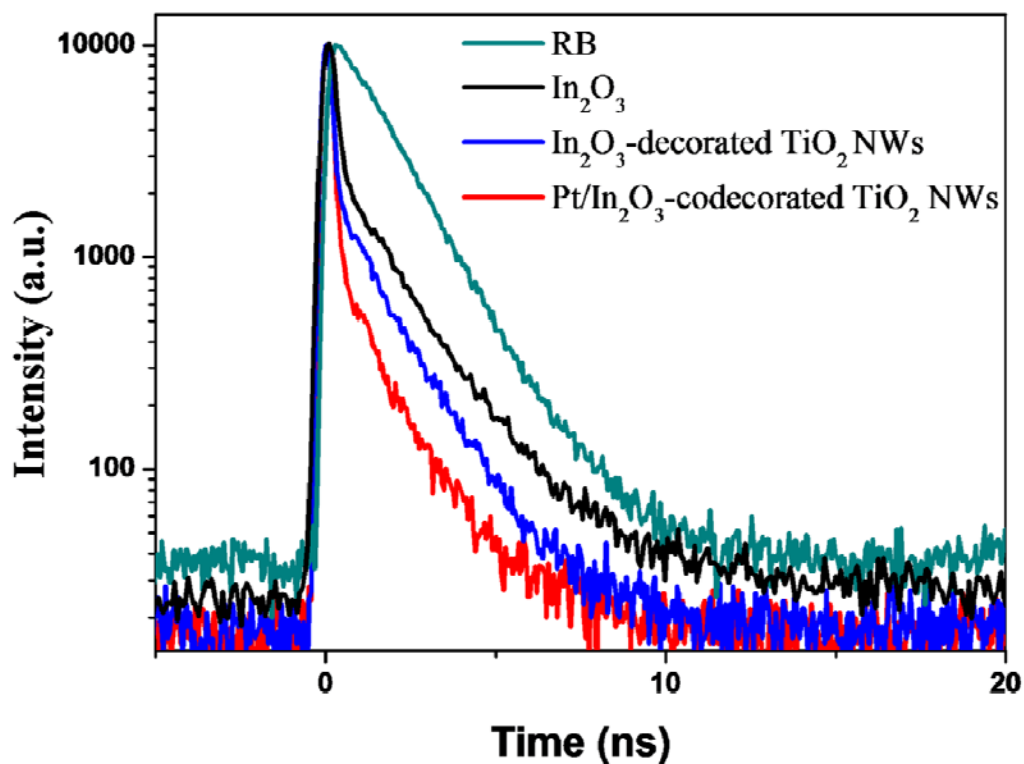
**Figure 3.10.2** Quenching of photoluminescence emission of RB Dye (donor) with different samples (acceptor).

Figure 3.10.3 shows the time-resolved PL spectra for the three RB solutions relatively containing  $\text{In}_2\text{O}_3$ ,  $\text{In}_2\text{O}_3\text{-TiO}_2$ , and  $\text{In}_2\text{O}_3\text{-TiO}_2\text{-Pt}$  NWs. The emission decay data were analyzed with biexponential kinetics in which two decay components were derived. The lifetimes ( $\tau_1$  and  $\tau_2$ ), pre-exponential factors ( $A_1$  and  $A_2$ ), and intensity-average lifetime ( $\langle\tau\rangle$ ) were determined and summarized in Table 1. The average lifetimes of  $\text{In}_2\text{O}_3$ ,  $\text{In}_2\text{O}_3\text{-TiO}_2$  and  $\text{In}_2\text{O}_3\text{-TiO}_2\text{-Pt}$  were 1.2171, 1.0472, and 0.6770 ns, respectively. Note that the difference in the average emission lifetime between  $\text{In}_2\text{O}_3\text{-TiO}_2$  ( $\langle\tau\rangle = 1.0472$  ns) and  $\text{In}_2\text{O}_3$  ( $\langle\tau\rangle = 1.2171$  ns) indicates the emergence of a nonradiative pathway from the interaction between  $\text{In}_2\text{O}_3$  and  $\text{TiO}_2$ . This proposition can be confirmed by the more pronounced emission quenching of RB observed for  $\text{In}_2\text{O}_3\text{-TiO}_2$  sample. Such difference became more noticeable as  $\text{In}_2\text{O}_3\text{-TiO}_2$  NWs were further decorated with Pt ( $\langle\tau\rangle = 0.6770$  ns for  $\text{In}_2\text{O}_3\text{-TiO}_2\text{-Pt}$  versus  $\langle\tau\rangle = 1.2171$  ns for  $\text{In}_2\text{O}_3$ ), inferring a much more significant electronic interaction between  $\text{In}_2\text{O}_3$  and  $\text{TiO}_2$ . If electron transfer was the predominant process that dictated the emission quenching of RB, we can then estimate the electron-transfer rate constants ( $k_{et}$ ) of  $\text{In}_2\text{O}_3\text{-TiO}_2$  and  $\text{In}_2\text{O}_3\text{-TiO}_2\text{-Pt}$  samples from the emission lifetime data by the following equations [45]:

$$k_{et,1} = \frac{1}{\langle \tau \rangle} (In_2O_3 - TiO_2) - \frac{1}{\langle \tau \rangle} (In_2O_3)$$

$$k_{et,2} = \frac{1}{\langle \tau \rangle} (In_2O_3 - TiO_2 - Pt) - \frac{1}{\langle \tau \rangle} (In_2O_3 - TiO_2)$$

Using the lifetime values listed in Table 1, we obtained the electron-transfer rate constants from  $In_2O_3$  to  $TiO_2$  ( $k_{et,1}$ ) and from  $TiO_2$  to Pt ( $k_{et,2}$ ) as  $0.13 \times 10^9$  and  $0.52 \times 10^9$   $s^{-1}$ , respectively. In addition, we noticed that the rate constant of  $k_{et,1}'$  ( $0.65 \times 10^9$ ) was larger than  $k_{et,1}$  ( $0.13 \times 10^9$ ), which means that the electron transfer from  $In_2O_3$  to  $TiO_2$  was faster in the  $In_2O_3$ - $TiO_2$ -Pt system. This result, together with those of photocatalysis, photocurrent measurement and PL quenching, confirms our suggestion that an increasing driving force of electron transfer from  $In_2O_3$  to  $TiO_2$  can be achieved by the decoration of Pt on the  $TiO_2$  region of  $In_2O_3$ - $TiO_2$  NWs.



**Figure 3.10.3** Time-resolved PL spectra of RB solutions containing In<sub>2</sub>O<sub>3</sub>, In<sub>2</sub>O<sub>3</sub>-TiO<sub>2</sub> and In<sub>2</sub>O<sub>3</sub>-TiO<sub>2</sub>-Pt samples.

**Table 1** Kinetic analysis of emission decay of RB in the presence of different samples.

system	$A_1$	$\tau_1$ (ns)	$A_2$	$\tau_2$ (ns)	$\langle \tau \rangle$ (ns)	$k_{\text{et}}$ ( $\text{s}^{-1}$ )
RB/ $\text{In}_2\text{O}_3$	3213.4	1.4048	6318	0.1224	1.2171	$k_{\text{et},1}=0.13 \times 10^9$
RB/ $\text{In}_2\text{O}_3$ - $\text{TiO}_2$	1995.1	1.4917	9259	0.1627	1.0472	
RB/ $\text{In}_2\text{O}_3$	3213.4	1.4048	6318	0.1224	1.2171	$k_{\text{et},1}'=0.65 \times 10^9$
RB/ $\text{In}_2\text{O}_3$ - $\text{TiO}_2$ - Pt	846	1.4454	11031	0.1665	0.6776	
RB/ $\text{In}_2\text{O}_3$ - $\text{TiO}_2$	1995.1	1.4917	9259	0.1627	1.0472	$k_{\text{et},2}=0.52 \times 10^9$
RB/ $\text{In}_2\text{O}_3$ - $\text{TiO}_2$ - Pt	846	1.4454	11031	0.1665	0.6776	

## Chapter 4. Conclusion

In this thesis, we have successfully synthesized  $\text{In}_2\text{O}_3$ -decorated anatase  $\text{TiO}_2$  NWs via a simple precipitation-annealing process. The difference in band structures between  $\text{In}_2\text{O}_3$  and  $\text{TiO}_2$  provided charge carriers with another preferential route for charge transfer, resulting in the separation of photoexcited electrons and holes. The charge carrier separation in  $\text{In}_2\text{O}_3$ - $\text{TiO}_2$  NWs was revealed with the photocatalytic decomposition of RB. As compared to the commercial P-25  $\text{TiO}_2$  powder and  $\text{In}_2\text{O}_3$ -loaded  $\text{TiO}_2$  NW samples, the as-synthesized  $\text{In}_2\text{O}_3$ - $\text{TiO}_2$  NWs exhibited superior photocatalytic efficiency under UV illumination, demonstrating their potential as an efficient photocatalyst in relevant redox reactions. A further enhancement in the photocatalytic activity of  $\text{In}_2\text{O}_3$ - $\text{TiO}_2$  NWs can be achieved when Pt nanoparticles of suitable amount were deposited on the surface of  $\text{TiO}_2$ . This improvement is due to the increasing driving force of electron transfer from  $\text{In}_2\text{O}_3$  to  $\text{TiO}_2$  achieved by the decoration of Pt on  $\text{TiO}_2$  surfaces. Time-resolved PL data showed that a higher electron-transfer rate constant from  $\text{In}_2\text{O}_3$  to  $\text{TiO}_2$  was observed for  $\text{In}_2\text{O}_3$ - $\text{TiO}_2$ -Pt NWs, consistent with the results of photocatalysis and photocurrent measurement. The current  $\text{In}_2\text{O}_3$ - $\text{TiO}_2$ -Pt

NWs may find promising photocatalytic applications, especially in the photocatalytic decomposition of various organic pollutants. The present study also gives rise to a new class of highly efficient metal/semiconductor hybrid photocatalysts which may effectively utilize the solar power.





# Reference

- [1] Zhu, J.; Yang, D.; Geng, J.; Chen D.; Jiang Z. *J. Nanopart. Res.* **2008**, *10*, 729.
- [2] Tang, H.; Berger, H.; Schmid, P. E.; Lévy, F. *Solid State Commun.* **1993**, *87*, 847.
- [3] Grätzel, M. *Nature.* **2001**, *414*, 338.
- [4] Duan, X.; Huang, Y.; Cui, Y.; Wang, J.; Lieber, C. M. *Nature (London)* **2001**, *409*, 66.
- [5] Yun, H. J.; Lee, H.; Joo, J. B.; Kim, W.; Yi, J. *J. Phys. Chem. C* **2009**, *113*, 3050.
- [6] Miao, L.; Tanemura, S.; Toh, S.; Kaneko, K.; Tanemura, M. *J. Cryst. Growth* **2004**, *264*, 246.
- [7] Cozzoli, P. D.; Kornowski, A.; Weller, H. *J. Am. Chem. Soc.* **2003**, *125*, 14539.
- [8] Zhang, Q.; Gao, L. *Langmuir* **2003**, *19*, 967.
- [9] Wang, Q.; Wen, Z.; Li, J. *Inorg. Chem.* **2006**, *45*, 6944.
- [10] Wu, J. M. *J. Cryst. Growth* **2004**, *269*, 347.
- [11] Wu, J. M.; Shih, H. C.; Wu, W. T. *Chem. Phys. Lett.* **2005**, *413*, 490.
- [12] Liu, S.; Huang, K. *Sol. Energy Mater. Sol. Cells* **2005**, *85*, 125.

- [13]Zhu, Y.; Li, H.; Kolytyn, Y.; Hacothen, Y. R.; Gedanken, A. *Chem. Commun.* **2001**, 2616.
- [14]Kasuga, T.; Hiramatsu, M.; Hoson, A.; Sekino, T.; Niihara K. *Langmuir* **1998**, *14*, 3160.
- [15]Kasuga, T.; Hiramatsu, M.; Hoson, A.; Sekino, T.; Niihara, K. *Adv. Mater.* **1999**, *11*, 1307.
- [16]Waclawik, E. R.; Frost, R. L.; Zhu, H. Y.; Morgan, D. L. *Chem. Mater.* **2008**, *20*, 3800.
- [17]Kukovecz, A.; Hodos, M.; Horvath, E.; Radnoczi, G.; Konya, Z.; Kiricsi, I. *J. Phys. Chem. B* **2005**, *109*, 17781.
- [18]Wang, H.; Shao, W.; Gu, F.; Zhang, L.; Lu, M.; Li, C. *Inorg. Chem.* **2009**, *48*, 9732
- [19] Kraeutler, B.; Bard, A. J. *J. Am. Chem. Soc.* **1978**, *100*, 4317.
- [20]Baba, R.; Nakabayashi, S.; Fujishima, A.; Honda, K. *J. Phys. Chem.* **1985**, *89*, 1902.
- [21]Kamat, P. V. *J. Phys. Chem. B* **2002**, *106*, 7729.
- [22]Kamat, P. V. *J. Phys. Chem. C* **2008**, *112*, 18737
- [23]Subramanian, V.; Wolf, E. E.; Kamat, P. V. *J. Am. Chem. Soc.* **2004**, *126*, 4943

- [24]Pu, Y. C.; Chen, Y. C.; Hsu, Y. *J. Appl. Catal. B-Environ.* **2010**, *97*, 389.
- [25]Liu, D.; Kamat, P. V *J. Phys. Chem.* **1993**, *97*, 10769.
- [26]Jitputti, J.; Suzuki, Y.; Yoshikawa, S. *Catal. Commun.* **2008**, *9*, 1265.
- [27]Sun, X.; Li, Y. *Chem. Eur. J.* **2003**, *9*, 2229.
- [28]For bulk fcc Pt,  $d(200) = 0.1985$  nm from JCPDS 88-2343.
- [29]For tetragonal anatase TiO<sub>2</sub>,  $d(200) = 0.1885$  nm from JCPDS 89-4921.
- [30]Bocarsly, A. B.; Cameron, R. E. *J. Am. Chem. Soc.* **1985**, *107*, 6116
- [31]Bocarsly, A. B.; Cameron, R. E. *Inorg. Chem.* **1986**, *25*, 2910.
- [32]Harada, M.; Einaga, H. *Langmuir* **2006**, *22*, 2371
- [33]Zheng, J.; Dickson R. M. *J. Am. Chem. Soc.* **2002**, *124*, 13982.
- [34]Hada, H.; Yonezawa, Y.; Yoshida, A.; Kurakake, A. *J. Phys. Chem.* **1976**, *80*, 2728.
- [35]Chan S. C.; Barteau, M. A. *Langmuir* **2005**, *21*, 5588.
- [36]Li, F. B.; Li, X. Z. *Chemosphere* **2002**, *48*, 1103.
- [37]Arabatzi, I. M.; Stergiopoulos, T.; Andreeva, D.; Kitova, S.; Neophytides, S. G.; Falaras, P. *J. Catal.* **2003**, *220*, 127.
- [38]Skriver, H. L.; Rosengaard, N. M. *Phys. Rev. B* **1992**, *45*, 9410.

- [39] Xu, Y.; Schoonen, M. A. A. *Am. Miner.* **2000**, *85*, 543.
- [40] Wang, E.; Yang, W.; Cao, Y. *J. Phys. Chem. C* **2009**, *113*, 20912
- [41] For cubic  $\text{In}_2\text{O}_3$ ,  $d(222) = 0.29211$  nm and  $d(211) = 0.41311$  nm from JCPDS 89-4595.
- [42] Martinez-de la Cruz A.; Garcia Perez, U. M. *Mater. Res. Bull.* **2010**, *45*, 135.
- [43] Xu, A. W.; Gao, Y.; Liu, H. Q. *J. Catal.* **2002**, *207*, 151.
- [44] Wen, D.; Guo, S.; Wang, Y.; Dong, S. *Langmuir* **2010**, DOI: 10.1021/la100869r, in press.
- [45] Yang, T. T.; Chen, W. T.; Hsu, Y. *J. Phys. Chem. C* **2010**, DOI: 10.1021/jp103294c, in press.

